BRAZILIAN CENTER FOR RESEARCH IN PHYSICS

GROWTH AND CHARACTERIZATION OF COBALT SULFIDE FILMS ON AU(100) BY SCANNING TUNNELING MICROSCOPY

BY: LUIZA DE OLIVEIRA SALIM JOSÉ

ADVISOR: DR. FERNANDO LOUREIRO STAVALE JUNIOR

A thesis submitted in partial fulfillment of the requirements for the degree of

MASTER OF PHYSICS

Rio de Janeiro, Brasil
July, 2026

"Growth and Characterization of Cobalt Sulfide films on Au(100) by Scanning Tunneling Microscopy"

LUIZA DE OLIVEIRA SALIM JOSÉ

Dissertação de Mestrado em Física apresentada no Centro Brasileiro de Pesquisas Físicas do Ministério da Ciência Tecnologia e Inovação. Fazendo parte da banca examinadora os seguintes professores:

Documento assinado digitalmente
gov.br FERNANDO LOUREIRO STAVALE JUNIOR
Data: 09/09/2026 12:47:26-0300
Verifique em https://validar.iti.gov.br

Fernando Loureiro Stavale Junior - Orientador/CBPF

Documento assinado digitalmente
gov.br BRUNA FERNANDA BAGGIO
Data: 20/08/2026 11:47:28-0300
Verifique em https://validar.iti.gov.br

Bruna Fernanda Baggio – CNPEM

Documento assinado digitalmente
gov.br EDMAR AVELLAR SOARES
Data: 31/08/2026 12:06:57-0300
Verifique em https://validar.iti.gov.br

Edmar Avellar Soares – UFMG

Rio de Janeiro, 23 de julho de 2026.

.

Your greatest enemy is your own mind. Master it, and you will be unstoppable.

ACKNOWLEDGMENTS

There is no other way to start this than by thanking God for everything. He works in mysterious ways, but how wonderful it is to be able to learn from His works.

Secondly, I thank my friends from UFSC: André, Jadna, Lucas, Mário, Vini, Laura, and Agatha. They pushed me to be a better physicist with their creative ways of solving problems and even crazier discussions. André and Jadna, our friendship began during the pandemic (even though we started college together one year before that), and I sincerely hope it will last a very long time. Thank you for all the jokes and deep conversations about life; I don't think I will ever be able to show you how much I appreciate you. Mário, my two-year partner during our undergraduate research project at LabSiN, I hope I have brightened your days as much as you have brightened mine.

I am truly grateful to my advisor, Fernando Stavale. He has taught me so much in so little time, and yet I feel I have even more to learn from him. To all my laboratory partners — Igor, Millena, Caique, Rodrigo, Malu, César and Rubem — Thank you for making my days lighter and definitely funnier. It was great sharing unique lunches and afternoon snack conversations with you. I believe I am a better person, both for myself and others, because of you. A special thank you to all security guards, maintenance personnel, students, researchers, and technicians, because this institution is only great due to all of their work and effort.

Another special person in my life is my German teacher, and later dear friend, Silvia, who watched me grow from a messy teenager to a proud physicist. Thank you for all the conversations in German and in Portuguese, for all the life advice, and for listening to me blurt out all the problems that actually didn't matter that much. I hope you are ready to listen to my complaints, expectations, and victories that the next chapter of my life will bring.

I could never forget to thank my family, especially my parents, Shirley and Rogério, and grandparents, Vó Lourdes, Vô Alamiro, Vó Lena and Vô Alexandre. They taught me what it means to love and support someone, even when they are thousands of kilometers away. It doesn't matter where I go; you will always be with me, and I will always be grateful for your care and your dedication to me and our family. I won't forget you, my brother-in-law, Rafael — don't worry. Thank you for being a principled man, a great professional, and for taking such good care of my sister. I admire you a lot.

Mom, Dad, thank you for giving me the greatest gifts I could have ever received: life and an older sister — a lifelong partner. Jujubs, I truly don't know who I would be without you. You have shown me love, support, and presence beyond anything I could have imagined, and I am sure life is not long enough for me to show you how much I love you and how much you mean to me. Thank you for holding my hand every time I needed it, and I hope you know I will always be here for you. You and I against the world!

The last person I need to thank is my boyfriend, Pablo. I could not be more grateful for all the help you have given me, even before we were together. You always believed in me more than I believed in myself. Thank you for all the time we spent together discussing physics, sharing problems and victories, listening to music, and having fun. You helped me become a better person and a better professional, and you showed me what it means to be fully dedicated to and completely in love with what you do. Your discipline, resilience, and effort are the three things I admire most about you. Thank you for filling my days with love and support. I love you.

Finally, I thank CAPES for funding this research, and Petrobras for trusting and supporting the Interface Group in carrying out projects of mutual interest, UFSC for providing me with a strong foundation in physics, and CBPF for showing me that great opportunities await us if we have the courage to pursue them.

Contents

List of Figures

Resumo

Os sulfetos metálicos são amplamente utilizados em tecnologias relacionadas à energia, como células solares, sensores de gás e eletrocatálise. Entre eles, o sulfeto de cobalto se destaca por sua elevada atividade catalítica, estabilidade térmica, abundância natural e baixa toxicidade. Para investigar sua estrutura atômica e organização superficial por Microscopia de Tunelamento por Varredura (STM), filmes finos de CoS_x foram crescidos sobre um monocristal de Au(100) em condições de ultra-alto vácuo. O estudo foi dividido em quatro etapas: (i) investigação da nucleação e dos estágios iniciais de crescimento do cobalto; (ii) análise da interação entre Au(100) e H_2S; (iii) desenvolvimento de diferentes rotas de preparação de filmes finos de CoS_x; e (iv) crescimento de sulfeto de cobalto por sulfurização de um filme pré-formado de óxido de cobalto. Através de Espectroscopia de Fotoelétrons Excitados por Raios-X (XPS), informações químicas das amostras produzidas foram obtidas e analisadas para determinar a composição dos filmes. Os resultados mostram que o cobalto nucleia preferencialmente nos sítios atômicos mais elevados da reconstrução da superfície Au(100), seguindo um mecanismo de crescimento tridimensional do tipo Volmer–Weber. A sulfurização do sistema Co/Au(100) em temperaturas acima de 423K levou a uma interdifusão significativa entre Co e Au, favorecendo a adsorção de enxofre sobre Au(100) e a possível formação de compostos do tipo Au_xS. Portanto, em razão da possibilidade de realizar a sulfurização em temperaturas mais baixas e da maior tendência à formação de um filme cristalino, um filme de $CoO(100)$ crescido sobre Au(100) foi sulfurizado a cerca de 500 K e resultou em uma superfície semelhante à de $Co_3S_4(111)$ apresentando um parâmetro de rede levemente expandido no plano.

Abstract

Metal sulfides are widely used in energy-related technologies such as solar cells, gas sensors, and electrocatalysis. Among them, cobalt sulfide stands out due to its high catalytic activity, thermal stability, abundance, and low toxicity. To investigate its atomic structure and surface organization by Scanning Tunneling Microscopy (STM), thin films of CoS_x were grown on an Au(100) single crystal under ultra-high vacuum conditions. The study comprised four stages: (i) investigation of cobalt nucleation and early growth; (ii) analysis of the interaction between Au(100) and H_2S; (iii) development of different preparation routes for CoS_x thin films; and (iv) growth of cobalt sulfide through sulfurization of a preformed cobalt oxide film. Through X-ray Photoelectron Spectroscopy (XPS), the chemical information about the prepared samples was obtained and analyzed to determine the film composition. The results show that cobalt nucleates on the highest atomic sites of the reconstructed Au(100) surface, following a three-dimensional Volmer-Weber growth mechanism. Sulfurization of Co/Au(100) at temperatures above 423 K led to significant Co-Au interdiffusion, favoring sulfur adsorption on Au(100) and possible formation of Au_xS compounds. Therefore, owing to the possibility of performing the sulfurization at lower temperatures and the greater tendency toward the formation of a crystalline film, a CoO(100) film grown on Au(100) was sulfurized at approximately 500 K and resulted in a cobalt sulfide continuous film with a Co_3S_4(111)-like surface and a slightly expanded in-plane lattice parameter.

Chapter 1

Introduction

The accelerated development of population, industry, and urbanization has generated a variety of significant consequences for the environment, such as water pollution and high energy consumption. In the last few decades, a variety of compounds have been widely studied to produce devices aiming to reverse the pollution (air, water, ...) in the environment and improve the current energy storage devices. Among these materials, metal sulfides (MS) structures have been attracting the interest of the surface community due to their potential for applications in the production of batteries [1–3], solar cells [4], supercapacitors [5, 6], electrocatalysts for the water splitting reaction for the production of green hydrogen [7, 8], sensors for gases and chemicals [9, 10], and photocatalysts for environmental remediation [11, 12]. This class of materials is composed of a sulfur anion (S^{-2}) linked to at least one cationic metal (M^{+n}) or semi-metal to form a M_xS_y compound with varying stoichiometry such as MS, M_2S, MS_2, and M_3S_4.

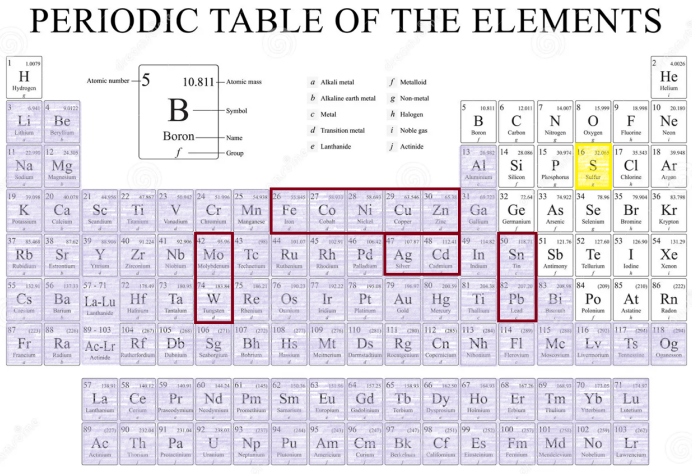

Figure 1.1: *Periodic table highlighting the elements that form metal sulfides, including those currently investigated for the formation of 2D materials.*

Figure 1.1 presents a periodic table in which metal elements are highlighted in lavender, sulfur is highlighted in yellow, and red rectangles indicate elements that form 2D materials that are currently the subject of extensive research.

Of particular interest in this work, cobalt sulfides have a special relevance due to their temperature stability, high activity, selectivity, abundance in nature and non-toxic properties [13]. Cobalt sulfide has a range of different stoichiometric compositions depending on Co:S ratio available (sulfur background pressure) and the heating temperature during synthesis. Fig 1.2 shows the phase diagram for the Co-S system, where the most stable phases are Co_9S_8, Co_3S_4 and CoS, in this order. In this diagram, the vertical axis indicates the temperature in Celsius and the horizontal axis indicates the sulfur content, expressed as atomic percentage on the bottom scale and weight percentage on the top scale. The left end of this diagram corresponds to pure cobalt.

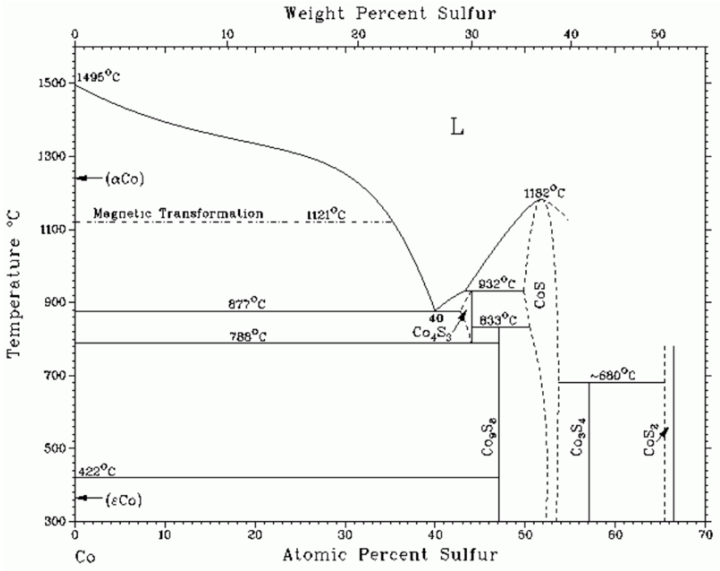

Figure 1.2: *Phase diagram for the Co-S system [2]*

CoS [14, 15] is known to have the same structure as NiAs, where cobalt is placed at the center of 6 sulfur atoms, forming a CoS_6 octahedron. CoS_2 shows a pyrite structure [14, 16], consisting of a face centered cubic structure of cobalt atoms surrounded by six sulfur atoms. This structure forms slightly distorted octahedra that share their corners. The Co_3S_4 crystallizes in the spinel structure [14], where cobalt sites show two different coordinations by sulfur: tetrahedral and octahedral. The CoS_6 octahedra share their corners with other octahedra while the CoS_4 tetrahedra are linked to the octahedra by their vertices. The Co_9S_8 structure [14, 16] has CoS_6 octahedra linked to CoS_4 tetrahedra by their vertices with some tetrahedral sites sharing their sides with other tetrahedra. The above-mentioned cobalt sulfide phases are illustrated in Fig. [1.3].

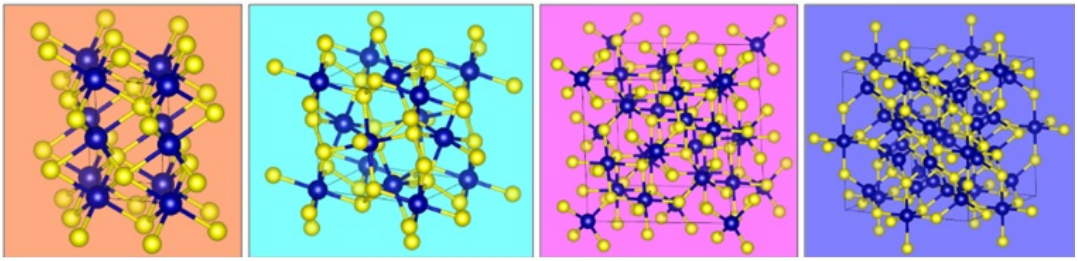

Figure 1.3: *Naturally occuring cobalt sulfide structures: (a) CoS with NiAs structure, (b) CoS_2 with pyrite structure, (c) Co_3S_4 with spinel structure and (d) Co_9S_8 structure. Figures generated using VESTA [17].*

The aforementioned applications of cobalt sulfide are highly dependent on the local structure arrangement, especially when working with catalysts and sensors, where the reactions occurring on the surface of the material control its efficiency. In this regard, Scanning Tunneling Microscopy becomes crucial to provide atomistic information regarding topography and insights on electronic structure configuration.

To provide a better understanding of the structure and atomic organization of cobalt sulfide films, this dissertation is organized as follows:

- Chapter 2 introduces the fundamental aspects of crystal structure, the structural and electronic properties of crystal surfaces, the basic principles of thin-film growth, and the theoretical background of STM and XPS;
- Chapter 3 presents a review of the most relevant literature to this study, focusing on cobalt evaporation by electron-beam evaporation, sulfurization of Au(100), cobalt oxide growth on Au(100), and, finally, cobalt sulfide growth on Au(100);
- Chapter 4 describes the experimental methods employed in this Master's research, providing details on the substrate used in this work, as well as the operation and calibration of the techniques and experimental systems employed;
- Chapter 5 presents the results, analysis, and discussion of the different series of experiments that led to the successful growth of cobalt sulfide on Au(100);
- Finally, Chapter 6 summarizes the main findings and discusses potential directions for future research.

This thesis concludes with an appendix describing the basic operation of the NANONIS Mimea interface, which was used to control and operate the Scanning Tunneling Microscope throughout the experiments presented in this work.

Chapter 2

Theoretical Background

2.1 Surfaces and Interfaces

A solid can be defined as a state of matter that has a determined shape and volume, composed of interfaces (the limits separating the solid from any other medium) and its interior (named bulk). By definition, if the limits of the solid material are in contact with the atmosphere or a vacuum environment, the interface is called surface, which consists of the last layers of atoms before the outside medium. In the field of surface science, the main interest is the study of the interactions, reactions, and changes that occur on the surface of a sample under investigation. Consequently, it is desirable to obtain a surface that is sensitive to the reactants involved in the process while exhibiting minimal contamination or impurities. To obtain a surface as close to an ideal one as possible, the samples must be treated with a special preparation process and under well-defined external conditions.

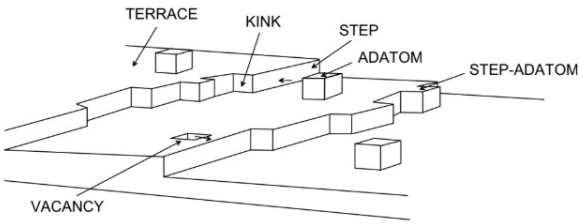

Figure 2.1: *Illustration of a real surface [18]*

Figure 2.1 illustrates a real surface, which is composed of terraces (large area with a flat surface), vacancies (missing atoms or groups of atoms), adatoms (atoms adsorbed on the surface), steps, step-adatoms (atoms that minimize their free energy by coupling to an already existing step) and kinks (irregularities that cause steps to be crooked instead of perfectly straight). When conducting surface

science research an ideal surface mainly composed of terraces is desirable due to its great uniformity and cleanliness. Although some characterization techniques, such as Scanning Tunneling Microscopy (STM), require atomically flat surfaces, others, such as Low-Energy Electron Diffraction (LEED) and X-ray Photoelectron Spectroscopy (XPS), impose less stringent requirements on surface flatness. The reason behind that is the level of insight each technique delivers, the STM is extremely sensitive to the smallest variation in a sample's surface due to the proximity between the tip and the sample and the tunneling current's strong dependence on the tip-sample distance. Meanwhile, LEED primarily probes the first few atomic layers due to the short inelastic mean free path of low-energy electrons, whereas XPS typically provides chemical information from a depth of a few nanometers. Consequently, neither LEED nor XPS are strictly limited to the outermost atomic layer of the sample.

In the majority of thin-film growth studies with STM the defined substrate is a single crystal due to its periodic arrangement of atoms being continuous and uniform throughout the entire solid, which results in a surface regularity that reflects this property. In this work, a single crystal was used as a substrate for the growth of CoS_x thin films.

2.1.1 Crystal structure

The arrangement of atoms in a crystal indicates the crystal structure, which is the infinite repetition of a group of atoms. This group is called the unit cell or the primitive cell, when it is composed of the smallest number of atoms that can describe the whole crystal. By placing side by side these unitary cells, we create the crystallographic lattice that can be defined in 3 dimensions by a set of three translational vectors:

$$\mathbf{r} = n_1 \cdot \mathbf{a}_1 + n_2 \cdot \mathbf{a}_2 + n_3 \cdot \mathbf{a}_3 \ . \tag{2.1}$$

This relation must be valid from all the points in the crystal that are translated an integer of any of the vectors **a**. Here n_1, n_2 and n_3 are integers that together with the vectors a_1, a_2 and a_3 define the crystal lattice.The magnitude of these vectors is called the lattice parameter. The crystal axes are usually chosen to be the axes defined by the primitive cell, but a different set of axes can be chosen for the crystal when it presents a simpler relation to the symmetry of the crystal. One can choose the primitive cell by choosing a lattice point in the structure and connecting it to all adjacent lattice points. By drawing a perpendicular line in the middle of each line connecting two lattice points, one obtains a geometric figure

made by the intersection of the lines. This volume constitutes the *Wigner-Seitz cell*.

There are seven types of crystal structures in three dimensions: cubic, tetragonal, orthorhombic, monoclinic, triclinic, trigonal and hexagonal. They are characterized by the equality or inequality between the magnitudes of the primitive vectors and the angles between them. From these seven crystal structures, fourteen different crystal lattices can be formed and they are called the *Bravais Lattices*.

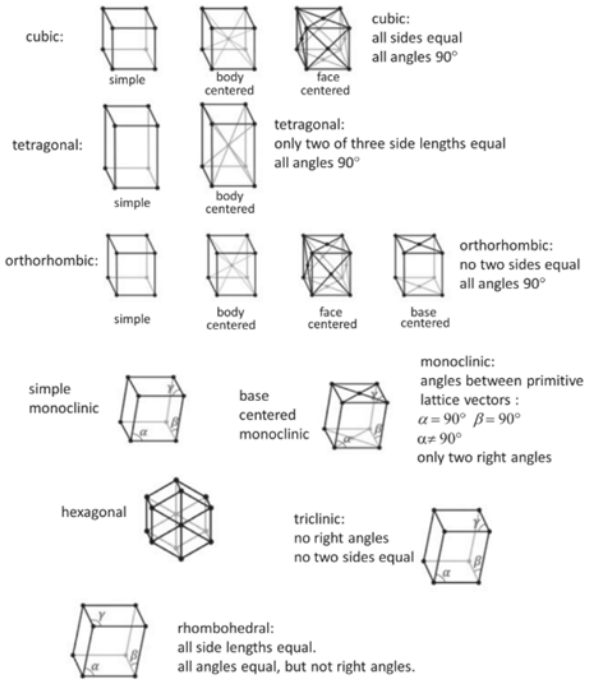

Figure 2.2: *Bravais Lattices from [19]*

Since we will discuss the structure of a gold single crystal and the metallic cobalt, the cubic and hexagonal lattices will be explained in detail. Three Bravais lattices present the cubic structure: face-centered cubic (FCC), Body-centered cubic (BCC) and simple cubic (SC). Although they all have their lattice vectors with the same magnitude and the angle between them is always 90°, only the simple cubic has the crystal axes matching the primitive axes. The gold single crystal utilized in this study has an FCC unit cell with a lattice parameter of $a = b = c = 2.95$ Å and 90° angles between its lattice vectors, while the cobalt crystal presents a temperature-dependent phase transition from Hexagonal close-packed (HCP) with lattice parameters $a = b = 2.50$ Å and $c = 4.03$ Å to Face-centered cubic (FCC) with lattice parameter $a = 3.55$ Å at $\sim 500K$. [20]

To identify the orientation of a crystal plane, it is necessary to specify three points inside the plane that are not collinear. If these three points are each in

a different axis of the crystal, we can write their coordinates as a multiple of the lattice constants. To obtain the index of a plane, firstly we must find the point where the plane intercepts each axis and write them in terms of the lattice constants a_1, a_2 and a_3. After that, we take the reciprocal of these number (the inverse) and, if they are fractions, we multiple by the minimum common divider of the three, resulting in three integers: h, k and l. The result written in closed parenthesis (hkl) is called the index of the plane and the three integers are called the *Miller indices*.

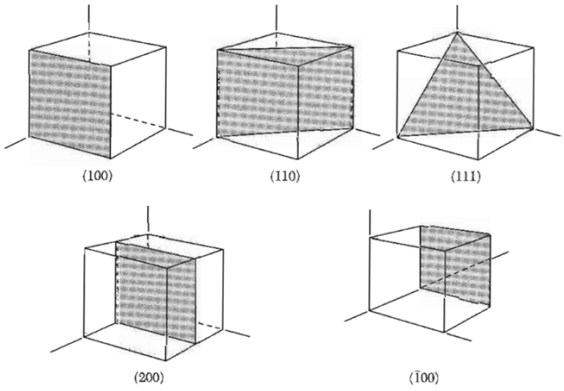

Figure 2.3: *Examples of common studied planes. Illustration from [21].*

For a Hexagonal Close-Packed structure, a fourth axis **c** can be included, normal to the other three axes, transforming the three Miller indices (hkl) into four Miller indices $(hkil)$, with the index i simply defined as $h + k = -i$.

Each crystal plane has a different composition and organization of atoms and, as a result, interacts with the same material in a distinct way. When working with a crystal, it is important to know and understand its plane structure and there are some techniques that allow us to identify it, such as the Low Energy Electron Diffraction (LEED). All techniques used to study crystal structures are based on the diffraction of photons, electrons or neutrons, which depends on the lattice constants of the crystal, since we must have the particle's wavelength comparable or smaller than the spacing of atoms in order to have diffraction beams and not ordinary optical refraction.

2.1.2 Structural and Electronic Properties of Crystal Surfaces

When a surface is created, the last layer is left with atoms that show an unsatisfied number of bonds due to the loss of an upper layer. These atoms, opposite to the bulk ones, are not neutral due to the existing of these dangling

bonds (unsatisfied bonds). There are two types of mechanisms that can lead the surface to the equilibrium of its charges: reconstruction or relaxation. The first one, reconstruction, is mostly seen in materials that have strongly directional bonds, such as tetrahedrically bonded semiconductors. Here the imbalance of charges can cause the atoms to move closer or away from others in a specific direction, breaking the translational symmetry of the surface, but resulting in no further modifications along the volume of the crystal. The second mechanism, relaxation, usually seen in simple metals in view of the delocalized electrons and chemical bonds present, does not change the translational symmetry. Instead, because there are no preferential direction in the organization of atoms but still a charge imbalance on the surface, the material relaxes by changing the vertical distance between layers of atoms.

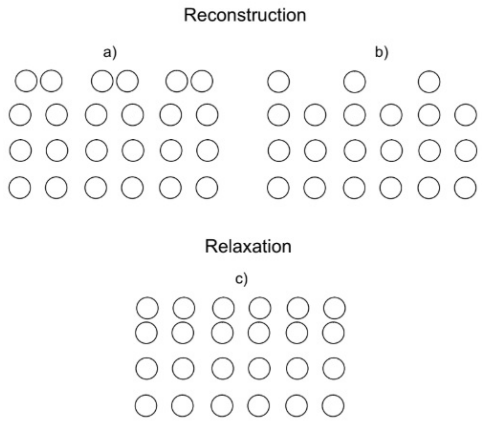

Figure 2.4: *Mechanisms for reaching surface equilibrium on a crystal: (a) and (b) shows 2 examples of reconstruction, and (c) shows the relaxation of a material. Illustration from [18].*

The topography of a surface can be investigated by Scanning Tunneling Microscopy (STM) when the relevant features are on the nanometer scale. For images acquired with atomic resolution, an intuitive interpretation would be that the observed contrast directly reflects contours of constant surface charge density. However, STM does not measure the charge density directly. Instead, the tunneling current depends strongly on the electronic structure of the sample and is approximately proportional to the integrated Local Density of States (LDOS) within the energy window defined by the applied bias voltage. Consequently, the contrast observed in STM images arises from a convolution of geometric and electronic effects, rather than exclusively from the surface topography.

The Local Density of States (LDOS), $n(E, x)$, is defined as the number of allowed states per unit energy range (DOS) spatially resolved, where each state's contribution is proportional to the density of its wave function $\phi(x)$ in a determined

point in space,

$$n(E,x) = \sum_j |\phi(x)|^2 \delta(E - \varepsilon_j). \tag{2.2}$$

Integrating this expression over x, we obtain a formula for the Density of States D(E):

$$D(E) = \frac{1}{V}\frac{dN(E)}{dE}, \tag{2.3}$$

where V is the volume of the system and $dN(E)/dE$ represents the number of states with energy between $E + \delta E$.

2.2 Thin-Films Growth

Before discussing thin-film growth modes, it is useful to review the fundamental principles of surface thermodynamics. A one-component system with N particles at a fixed temperature T and pressure p achieves its equilibrium when the free Gibbs energy $G(T,p,N)$:

$$G(T,p,N) = F + pV, \tag{2.4}$$

is minimized, with F being the Helmholtz free energy $F(T,V,N)$:

$$F(T,V,N) = U - ST. \tag{2.5}$$

It is related to the internal energy $U(S,V,N)$ and the entropy S by a Legendre Transformation. For an infinitesimal change in the internal energy, dU, the second law of thermodynamics can be written as

$$dU = TdS - pdV + \mu dN, \tag{2.6}$$

where μ is the chemical potential. Transformations in a system occurring at a constant temperature T, volume V and chemical potential μ can be described by the grand potential Ω, which is defined in terms of G and F as

$$\Omega = F - G = -pV. \tag{2.7}$$

For homogeneous microscopic systems, the Gibbs free energy can be written as a function of the extensive variable μ:

$$G = \mu N. \tag{2.8}$$

To begin the discussion about surface thermodynamics, we will use the Gibbs'

picture of a dividing surface [18]. Suppose two homogeneous phases, V_1 and V_2, separated by an inhomogeneous region, V_S, with its spatial extend being in the range of a few atomic layers. The two homogeneous phases are defined as the bulk solid and the vapor phase, respectively, while the inhomogeneous region is characterized by a gradually change in the particle density between the two phases (a transition region), as illustrated in Figure (2.5).

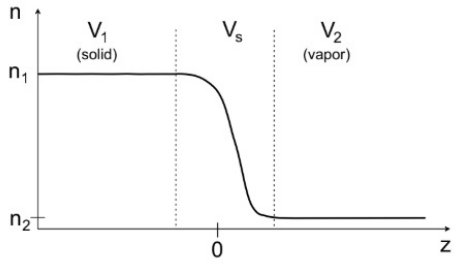

Figure 2.5: *Gibb's dividing surface described as a graphic of particle density $n = \frac{N}{V}$ as a function of the distance normal to the surface. Adapted from [18].*

The system, composed of the solid phase, the surface and the vapor phase, has a total volume V and number of particles N of

$$V = V_1 + V_2 \tag{2.9}$$

and

$$N = N_1 + N_2 + N_S. \tag{2.10}$$

Since the surface was defined as a plane, its volume is $V_S = 0$. For the sake of simplicity let us consider the number of particles in the surface negligible when compared to the whole system, thus $N_S = 0$. The grand potential Ω is written as a function of the two volumes, V_1 and V_2, and a term, Ω_S, that expresses the contribution from the surface:

$$\Omega = -p(V_1 + V_2) + \Omega_S. \tag{2.11}$$

The surface term Ω_S is proportional to the surface area as

$$\Omega_S = \gamma A, \tag{2.12}$$

where γ can be defined as the surface excess energy per unit area. From Gibb's assumption, $N_S = 0$, the surface contribution to the free Gibb's energy is neglected ($G_S = 0$), and the surface term in the expression for the grand potential becomes:

$$\Omega_S = F_s = \gamma A, \tag{2.13}$$

where F_S is the surface free energy. The surface excess free energy γ is defined as the characteristic free energy to create an additional piece of surface and can be expressed in terms of the surface free entropy S_S and the surface internal energy U_S as

$$\gamma = \frac{U_S - TS_S}{A}. \tag{2.14}$$

For crystalline solids, the existence of a preferential direction of cleavage results in different surface energies for distinguished facets of the crystal. That can be understood by the formation of dangling bonds due to the creation of a surface, which may leave a plane with a surface termination that is energetically unfavorable. As illustrated with Fig. 2.4, sometimes energetically unfavorable surface terminations are allowed to relax or reconstruct, evolving evolving toward a minimization of its surface free energy. Hence, area A should be defined as $A(h,k,l)$ due to its strong dependence on the crystallographic orientation of the sample and 2.14 becomes:

$$\gamma(h,k,l) = \frac{U_S - TS_S}{A(h,k,l)}. \tag{2.15}$$

By analyzing the surface free energy F_S two different contributions are found. For an infinitesimal variation in the surface free energy, two distinguished physical contributions appear:

$$dF_S = \gamma dA + Ad\gamma. \tag{2.16}$$

The first term is related to a change in the surface area, which can be achieved by increasing the number of atoms in the surface by a fixed averaged area per surface atom. The second term expresses an elastic deformation, where the number of surface atoms remains constant but the interatomic distance between them vary, creating an $d\gamma$ variation in the surface excess free energy. In a crystalline solid, distinct surfaces will show distinct surface free energies due to a range of surface effects, which results in the surface free energy having a direct dependence on the crystal plane analyzed.

An extensive area of surface physics is the study of thin film growth on crystalline surfaces, aiming to obtain a highly organized film. A thin film can be defined as a microscopic layer of material with thickness ranging from Angstroms (a monolayer) to micrometers. There are two ways of growing a film: by chemical vapor deposition (CVD) or by physical vapor deposition (PVD). As the names suggest, in the first one, the system evolves into chemical transformation (for example, two vapor reagents react and the product sublimates over a heated substrate [22]). In the second one, the system evolves into physical transformation (for example, by sublimation of a evaporated material [23]).

During the initial stages of film deposition, individual atomic processes can determine the mode of film growth, such as surface diffusion, nucleation and inter-diffusion of atoms. Phenomenologically, there are three distinct modes of film growth: layer-by-layer growth mode or Frank-van der Merwe, layer-plus-island growth or Stranski-Kastranov and island growth mode or Volmer-Weber. The first happens when the interaction between substrate atoms and layer atoms is stronger than the one between neighboring layer atoms. The last one is the opposite, occurs when the neighboring atoms of the adlayer have a stronger interaction than the one between the substrate and layer atoms. The Stranski-Kastranov is an intermediate case, where island growth begins after one or many layers are fully grown over the substrate surface.

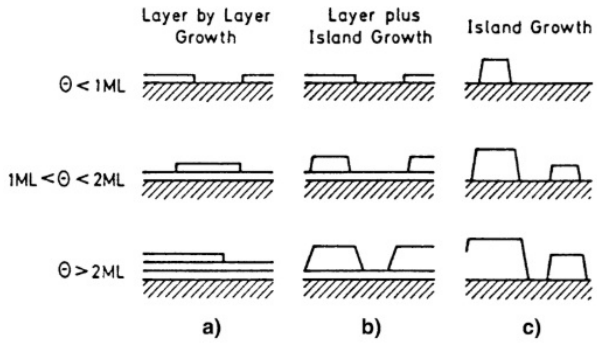

Figure 2.6: *Films growth modes: (a) layer-by-layer or Frank-van der Merwe mode, (b) layer-plus-island or Stranski-Kastranov growth and (c) island growth or Volmer-Weber mode. Illustration from [24].*

Applying the concepts of surface thermodynamics reviewed above, a formal distinction for the conditions met to have different modes of film growth can be defined. Since the surface free energy γ can also be interpreted as a force per unit length of boundary, the equilibrium of forces in the point where the surface and a 3D island of a deposited material connect results in the expression:

$$\gamma_s = \gamma_{s/f} + \gamma_f cos(\phi), \tag{2.17}$$

where γ_s represents the surface free energy between the substrate surface and vacuum, γ_f is the surface free energy between film and vacuum, $\gamma_{s/f}$ is the surface free energy between substrate and film and ϕ is the angle between the substrate surface and the film surface, as illustrated below.

From equation 2.17, we can distinguish between the 2D and 3D type by the angle ϕ. A layer-by-layer growth (Frank-van der Merwe growth) will have $\phi = 0$ and $\gamma_s \geq \gamma_{s/f} + \gamma_f$, in contrast with an island growth (Volmer-Weber growth) that has $0 \leq \phi \leq \frac{\pi}{2}$ and $\gamma_s < \gamma_{s/f} + \gamma_f$. The intermediate case, the Stranski-Kastranov

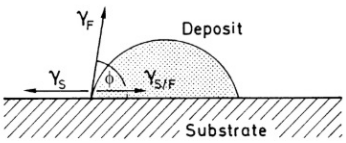

Figure 2.7: *Representation of 3D island growth on a substrate surface. Illustration from [24].*

growth, can be explained by an elastic deformation of the film due to a lattice mismatch between the substrate and the deposited film. The change from layer to island growth in this situation happens when the range of elastic strain field becomes larger than the effective range over which the adhesion force can keep neighboring atoms together. To minimize the surface free energy, the system roughens by growing in 3D islands.

On order to encompass the total system, which includes the vapor phase above the deposited film, we must incorporate the contribution from the variation on the free Gibbs enthalpy $\Delta G = N\Delta\mu$ when a particle in the gas phase is transferred to the condensed phase of the film. If the transition from the gas phase to the condensed phase happens at the equilibrium vapor pressure p_0, then no extra energy is required to this reaction since $\mu_{solid} = \mu_{gas}$. In the other hand, if this transition occurs at any other pressure $p \neq p_0$, a change in the free enthalpy can be described as

$$\Delta G = N k_B T \ln\left(\frac{p}{p_0}\right). \tag{2.18}$$

The ratio $\zeta = \frac{p}{p_0}$ is called supersaturation and it is defined as one of the driving forces for the deposition of a thin film from vapor pressure. Taking the vapor contribution into account, the new expressions for the condition for 2D and 3D growth modes become, respectively:

$$\gamma_s \geq \gamma_{s/f} + \gamma_f + C\ T \ln\left(\frac{p_0}{p}\right) \tag{2.19}$$

and

$$\gamma_s < \gamma_{s/f} + \gamma_f + C\ T \ln\left(\frac{p_0}{p}\right), \tag{2.20}$$

where C is a constant. with increasing supersaturation, layer-by-layer growth is favored. In vacuum deposition, the transition of particles from the vapor phase to the condensed deposited film is described by an impinging rate, expressed as

$$r = p_0\sqrt{2\pi M k_B T_0}, \tag{2.21}$$

that indicates the number of particles per cm^2 per second that arrive at the sub-

strate surface. In this expression, p_0 is the vapor pressure of the deposited material, M is the molecular weight of the deposited particles, k_B is the Boltzmann constant and T_0 is the temperature of the source.

The above-mentioned thermodynamic explanation of thin film growth is a simplification of the processes that compose this interaction between substrate and evaporant and, therefore, will relate to the section of evaporation of cobalt by MBE, but cannot be used to explain the growth of cobalt oxide and cobalt sulfide due to the increased complexity of those systems.

2.3 E-beam Evaporator

The electron-beam evaporator operates by using a focused electron beam to locally heat the material, promoting evaporation from its surface. The evaporant is placed inside a crucible (usually made of tungsten, boron nitride or graphite) that is bombarded by electrons. Behind the crucible, a current flowing through a filament results in the emission of electrons through the thermionic effect and these electrons are focused on the evaporant material by a high voltage and a magnetic field applied, which bends the electron beam through Lorentz force. The electrons' high kinetic energy is then partially transferred to the crucible in the form of heat, resulting in the sublimation of the evaporant material. Because the crucible is heated to extremely high temperatures (on the order of 1000°C), the system must be cooled by a continuous flow of water during operation.

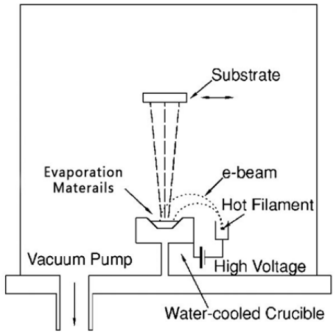

Figure 2.8: *Scheme of electron beam evaporation. Adapted from [25].*

2.4 Scanning Tunneling Microscopy

2.4.1 Quantum Tunneling

The physical concept behind Scanning Tunneling Microscopy is the tunneling effect, characterized by the tunneling of electrons through a potential barrier

(in this scenario, the vacuum between the tip of the microscope and the sample) because of the quantum nature of the electron. The simplest scenario is an electron tunneling through a rectangular potential barrier in one dimension (Fig. 2.9), where there are three different regions of potential: Region I has $V(x) = 0$ for $x < 0$; Region II has $V(x) = V_0$ inside the interval $0 < x < a$; and Region III has $V(x) = 0$ for $x > a$. The solution for this system is obtained from Schrödinger's equation in 1D:

$$i\hbar\frac{\partial\Psi(x,t)}{\partial t} = -\frac{\hbar^2}{2m}\frac{\partial^2\Psi(x,t)}{\partial x^2} + V(x)\Psi(x,t). \tag{2.22}$$

Since the Hamiltonian ($H = V(x) - \frac{\hbar^2}{2m}\frac{\partial^2}{\partial x^2}$) in this case is independent of time, we can write $\Psi(x,t)$ as the multiplication of two distinct functions, $\varphi(x)$ and $\tau(t)$, equation 2.22 can be solved separately for each variable. From here, it is easy to obtain the solution for the time part

$$-i\hbar\frac{\partial\tau(t)}{\partial t} = E\tau(t). \tag{2.23}$$

Since we are interested in the tunneling effect, we will study the position solution in more detail. The Schrödinger's equation independent of time in one dimension becomes:

$$-\frac{\hbar^2}{2m}\frac{d^2\Psi(x)}{dx^2} + V(x)\Psi(x) = E\Psi(x), \tag{2.24}$$

where $\Psi(x)$ is the electron's wave function, E the electron's energy, m the electron's mass and $\hbar$ the Planck's constant.

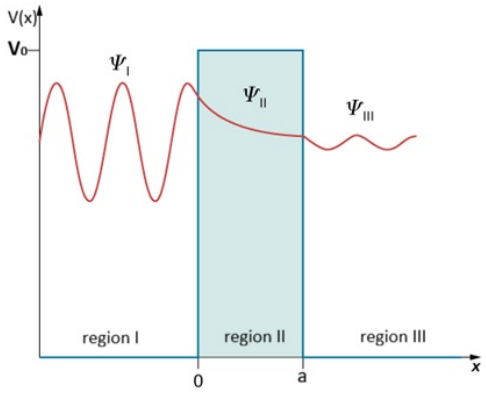

Figure 2.9: *Scheme of an electron tunneling through a one-dimensional square potential barrier*

For the regions where $V(x) = 0$, $x < 0$ (2.25) and $x > a$ (2.26), the electron's wave function is, respectively [26]:

$$\Psi_I(x) = Ae^{ikx} + Be^{-ikx} \tag{2.25}$$

and

$$\Psi_{III}(x) = A'e^{ikx} + B'e^{-ikx}, \tag{2.26}$$

for $k = \frac{\sqrt{2mE}}{\hbar}$. And for $V = V_0$, the solution is

$$\Psi(x)_{II} = Ce^{ik'} + De^{-ik'}, \tag{2.27}$$

where $k' = \frac{\sqrt{2m(V_0-E)}}{\hbar}$. Here A, B, A', B', C, and D are constants, k and k' are wave numbers, E is the electron's energy and V_0 is the potential barrier height. Each constant in one wave function predicts the existence of a wave moving forward (for example, constant A) and backward (constant B) in the direction of propagation. In the situation of an electron tunneling through a potential barrier, in region III, there won't be a wave moving in the opposite direction of propagation, which implies that $D = 0$. To obtain the other constants, we can apply the equation of continuity for the wave functions and their first derivatives for $x = 0$,

$$\Psi_I(x = 0) = \Psi_{II}(x = 0)$$

and

$$\left.\frac{\partial\Psi_I(x)}{\partial x}\right|_{x=0} = \left.\frac{\partial\Psi_{II}(x)}{\partial x}\right|_{x=0}. \tag{2.28}$$

For $x = a$,

$$\Psi_{II}(x = a) = \Psi_{III}(x = a)$$

and

$$\left.\frac{\partial\Psi_{II}(x)}{\partial x}\right|_{x=a} = \left.\frac{\partial\Psi_{III}(x)}{\partial x}\right|_{x=a}. \tag{2.29}$$

From these constants, it is possible to find the transmission probability ($T = |t|^2$, where t is the transmission coefficient), which gives information about the probability of the electron tunneling through the barrier, and the reflection probability ($R = |r|^2$, where r is the reflection coefficient), which informs about the probability of the electron not crossing the barrier. They are complementary and defined as [27]:

$$T = \frac{|C|^2}{|A|^2} = \left[1 + \frac{(k^2 + k'^2)^2 sinh^2(k'a)}{4k^2k'^2}\right]^{-1}, \tag{2.30}$$

with

$$R = \frac{|B|^2}{|A|^2} = 1 - T. \tag{2.31}$$

In the limit where $V_0 >> E$, $k'a >> 1$, the probability of tunneling is very low ($T << 1$) and we can simplify the expression for the transmission probability to

[27]

$$T = \frac{16k^2k'^2}{(k^2+k'^2)^2}e^{-2k'a}. \tag{2.32}$$

The tunneling current I_T will be proportional to the transmission probability T, the applied bias in the sample eV and the density of states of the sample at the Fermi edge $\rho_S(E_F)$ [26],

$$I_T \propto eV\rho_S(E_F)T \rightarrow I_T \propto eV\rho_S(E_F)e^{-\frac{\sqrt{8m(V_0-E)}}{\hbar}a}. \tag{2.33}$$

From equation 2.33 the sensitivity and power of this technique is exposed, even in a simple calculation. Due to the exponential dependency of the distance between the sample and the tip, the width of the barrier a, a slight change in the tip-sample distance generates a significant variation of the tunneling current between the two of them and the tunneling current is directly proportional to the applied bias.

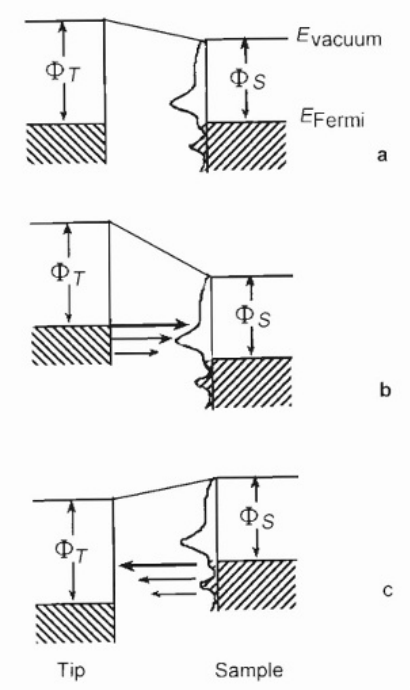

Figure 2.10: *Representation of the energy states of the sample and the tip when a bias is applied in the sample. (a) No bias applied, no current noticed. (b) $V_{bias} > 0$ applied to the sample, tunneling from occupied tip states to unoccupied sample states. (c) $V_{bias} < 0$, tunneling from occupied sample states to unoccupied tip states. Illustration from [28].*

2.4.2 Principles of Operation

While the tip and the sample are maintained in the same potential, there will be no significant tunneling current, because the Fermi level of both line up. When

a bias is applied to the sample, while maintaining the tip grounded, a tunneling current appears due to the difference between the sample and the tip Fermi Energy, which is the energy of the most energetic occupied state of a system. A positive sample bias results in a tunneling of electrons from the tip occupied states to the sample unoccupied states, meanwhile a negative bias applied to the sample results in a tunneling current flowing from the occupied states of the sample to unoccupied states of the tip. The potential barrier consists of the work functions of the tip, Φ_T, and the sample, Φ_S, and the Fermi Energy, E_F. Thus, it is safe to conclude that the electrons that participate in the tunneling current measured by the Scanning Tunneling Microscope are the ones in the states with energy between the Fermi Energy E_F and $E_F + eV$, where eV is the bias applied in the sample.

A more sophisticated approach can be obtained by the Tersoff-Hamann model. Tersoff and Hamann showed that equation 2.33 can be applied for a 3D scenario when it is assumed that the tunneling tip wave function can be approximated to a spherical *s-wave* and $\rho_S(E_F)$ is the local density of states of the sample at the Fermi edge at a distance of $s + R$, where s is the distance between the pinnacle of the tip and the surface and R is the radius of the tip's curvature.

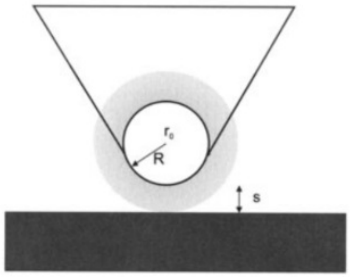

Figure 2.11: *Tersoff-Hamann model. Illustration from [26].*

This model is based on the Bardeen's Hamiltonian approximation. Bardeen demonstrated that the tunneling of electrons between two electrodes separated by an insulating material could be calculated by [26]

$$I_T = \frac{4\pi e}{\hbar} \int_{-\infty}^{\infty} [f(E_F - eV + \epsilon] - f(E_F + \epsilon)]\rho_S(E_F - eV + \epsilon)\rho_T(E_F + \epsilon)M^2 d\epsilon, \quad (2.34)$$

where $f(E)$ is the Fermi function, ρ_S and ρ_T are the density of states of the sample and the density states of the tip, eV is the applied voltage in the sample, M is the tunneling matrix element, e is the electron charge and ϵ is an integration variable. What is usually called the "Bardeen's approximation" lies in the equation used to obtain the tunneling matrix element, where Bardeen showed that the problem

can be solved for the tip and the sample waves separately[26]:

$$M = \frac{\hbar}{2m} \int_{surface} \left(\psi_S^* \frac{\partial \psi_T}{\partial z} - \psi_S \frac{\partial \psi_T^*}{\partial z} \right) dS, \tag{2.35}$$

where ψ_S and ψ_T are the wave functions of the sample and the tip, respectively. For low voltages applied, equation 2.34 can be written as [26]

$$I_T = \frac{4\pi e}{\hbar} \int_0^{eV} \rho_S(E_F - eV + \epsilon)\rho_T(E_F + \epsilon)M^2 d\epsilon. \tag{2.36}$$

And for a flat LDOS of the tip, meaning that ρ_T is constant over the analyzed energy interval, we obtain [26]

$$I_T \propto V\rho_S(E_F + eV). \tag{2.37}$$

This equation states that the tunneling current depends essentially on the LDOS of the sample at the Fermi energy.

2.5 X-ray Photoelectron Spectroscopy

2.5.1 Photoelectric Effect

X-ray Photoelectron Spectroscopy works through the Photoelectric Effect described by Albert Einstein in his 1905 paper "On a Heuristic Viewpoint Concerning the Production and Transformation of Light", which awarded him the Nobel Prize in Physics in 1921.

The photoelectric effect happens when an electromagnetic radiation falls on the surface of a material, causing the photon energy $E_f = h\nu$ to be absorbed by an electron of the material. If this energy is greater than the binding energy holding this electron in the atom, the electron is ejected with a characteristic kinetic energy K_e defined by equation 2.38 [29]:

$$K_e = h\nu - E_B - \phi, \tag{2.38}$$

where E_B is the Binding Energy of the electron, h is Planck's constant, ν is the frequency of the photon and ϕ is the work function of the material relative to the vacuum level. For the XPS, this equation becomes [29]

$$K_e = E_B - h\nu - \phi_{spect}, \tag{2.39}$$

where the work function above is the spectrometer's work function, because the binding energy obtained with XPS is measured with respect to the sample's Fermi Level, as shown in the energy diagram of Fig. 2.12.

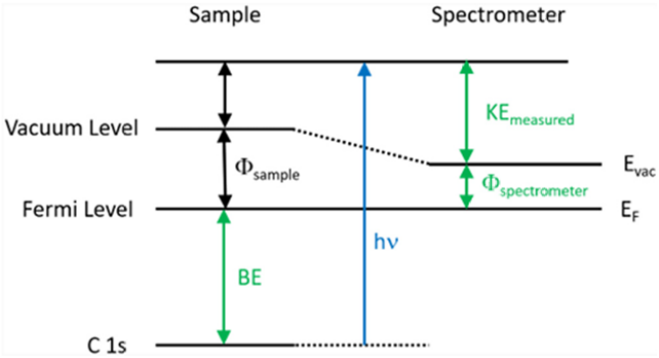

Figure 2.12: *Energy diagram explaining the Photoelectric effect equation using the C 1s level as an example. Scheme from [29].*

When the sample is irradiated with soft X-rays (energy less than 6keV), photons will excite electrons from the sample, but these electrons may not reach the analyzer. There are three ways an electron can react when it is excited by an X-ray: First, the electron can be emitted without interacting with the material (A); Second, the electron can collide with other particles of the sample and be ejected with a different energy than the expected by its binding energy (B); Lastly, the electron can collide with multiple particles of the material and not be ejected (C). XPS is characterized as a surface technique due to the fact that only the first tens of nanometers will be able to eject electrons without losing too much energy through collisions with neighboring atoms (A and B from Fig. 2.13).

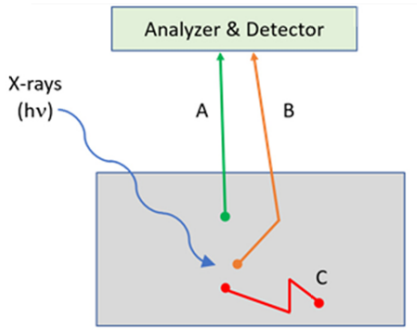

Figure 2.13: *Illustration from [29] showing the different interactions between the excited electron and the material. In (A), the electron excited by the X-ray is emitted without interacting with the sample, being detected by the XPS; in (B), the excited electron interacts inelastically with another particle, it is ejected and detected by the XPS, composing the XPS background; and, in (C), the excited electron interacts inellastically many times, not being emitted by the sample.*

After the emission of an electron, there are two different ways an atom can return to its fundamental state: by emitting x-ray fluorescence or an Auger elec-

tron. The latter is detected by XPS. As can be seen by the diagram in Figure 2.14, the x-ray fluorescence consists of an electron decaying from a higher electronic level which results in the emission of another photon with different energy, while the emission of an Auger electron consists of an electron decaying from a higher electronic level followed by the emission of an electron from a different electronic level.

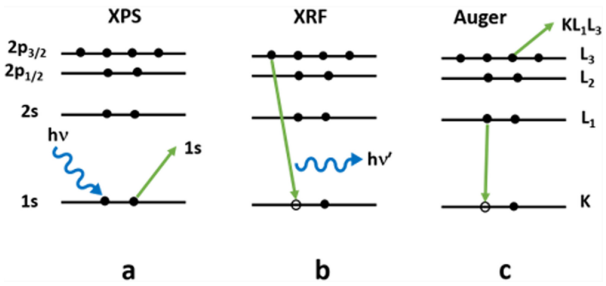

Figure 2.14: *Diagram showing the effects of bombarding a sample with X-rays: (1) Photoelectron emission, (2) X-ray Fluorescence emission and (3) Auger electron emission. Scheme from [29].*

Chapter 3

Literature Review

3.1 (Ultra)Thin Cobalt films on Au(100)

The deposition of transition metals by electron-beam evaporation is a well-established approach for the preparation and investigation of thin films. The choice of substrate plays a crucial role in determining the growth mode of the deposited material, particularly due to the possible lattice mismatch between the evaporant and the substrate surface. In the literature, cobalt film growth has been investigated on a variety of single-crystal substrates, including Au [30–34], Cu [35], Pd [36], and Pt [37–39]. Since Au(100) was used as the substrate in the present work, the literature review focuses on studies of cobalt growth on this particular single crystal.

A study of ultrathin cobalt films on Au(001) [this nomenclature is equivalent to Au(100) in terms of surface organization, with the alternative designation reflecting solely the author's choice of nomenclature] by *Katayama et al.* using RHEED (Reflection High Energy Electron Diffraction) experiments [40] showed that cobalt films up to 1 nanometer thick had a bcc structure, while films with thickness greater than 1nm appeared with hcp structure. Together with the previously reported temperature-dependent structure transition of cobalt [20], the growth of cobalt-based films is strongly dependent on the experimental conditions.

Studies found in the literature focused on the analysis of films less than 1 nm thick by imaging the as-grown bcc-Co films at RT and the post-annealed films [30, 31, 34]. By STM images, it was found that bcc-Co films have a monolayer apparent height of 1.40-1.50 Å with grainy but atomically flat first layer islands appearing as elongated rectangles with longer sides oriented parallel to the <110> direction of gold. As the film grew thicker, a coalescence of the second layer was

observed as a third layer started to nucleate before the completion of the second layer, indicating a low mobility of cobalt adatoms at RT. Thus it is confirmed by the literature that the RT growth of cobalt films on Au(001) is dominated by a Volmer-Weber (VW) growth mode, which is expected by the difference between surface free energy of Co and Au ($\gamma_{Co} = 2.7 J/m^2$ and $\gamma_{Au} = 1.6 J/m^2$) [41].

After annealing the samples at 500K, the irregular and discontinuous islands turned into regular nanostructures, indicating the activation of diffusion mechanisms. All papers [30–32] reported the appearance of the same structures: (1) reconstructed structures, (2) smaller unreconstructed rectangular regions on the Au(001)-(5x28) reconstructed surface, and (3) large terraces of reconstructed gold. Different authors reported that the area of islands (1) increased with increasing cobalt coverage, while the area of islands (2) decreased, which led them to conclude that islands (1) were associated with cobalt. The apparent height of islands (1) was 1.0Å with its rim having a slight bump of 0.6Å, while islands (B) showed an apparent height of 1.6Å and structure (3) had the characteristic 2.0Å apparent height of gold with the 14.4Å periodicity of its reconstruction. Islands (1) and (2) have apparent heights that clearly differ from bcc-Co or even fcc-Co (expected to be similar to gold, 2.0Å). The proposed model from *Kawagoe et al.* [31] suggests that the cobalt islands are embedded on the substrate with a surfactant Au overlayer. This hypothesis is consolidated by Scanning Tunneling Spectroscopy (STS) measurements that showed no significant difference between the Au(100) reconstructed region and the unreconstructed one, and by theoretical studies that indicated that a burrowing of cobalt atoms on gold was thermodynamically favorable due to a weak attractive interaction between Co atoms in the surface, resulting in the decrease of the total energy of the system [42].*Kawagoe et al.* [42] suggested that the islands with height of 1.0 Å were composed of 5ML bcc-Cobalt with 1ML Au on top with its rims consisting of 4ML bcc-Co and 2ML gold on top and the ones with height of 1.6 Å were 4ML bcc-Co with a gold monoatomic overlayer. *Unguris et al.*[43] showed that the gold reconstruction is seen only for more than 4ML thick Au, suggesting that the thickness of the surfactant overlayer could be estimated by the height difference between the reconstructed and unreconstructed islands.

These samples were also studied by Low-Energy Electron Diffraction (LEED) experiments [30, 32] before annealing, where a p(1×1) pattern, with the cobalt surface mesh showing a lattice constant of 2.85 Å, was found for films with thickness up to 2.4ML, with the 1.0ML thin film being the one with sharpest LEED pattern, indicating that thicker films exhibit poor medium and long-range order. *Kawagoe et al.*[30] reported a (2×1) LEED pattern for post-annealed bcc-Co films

with a thickness of 3.4ML, for which STM showed a structure with fine stripes distancing from each other by 5.7 Å. It was suggested by the authors that this structure consists of 5ML Cobalt with 1ML of the (2×1) structure, which the authors indicated might be due to a surface-ordered alloy.

3.2 Sulfurization of Au(100)

The literature reports studies on the sulfurization of Au(111) [44–46], Au(100) [47–49], and Au(110) [50, 51]. Since Au(100) was used as the substrate in the present work, the literature review focused on studies involving this particular surface orientation.

Previously reported studies of sulfide adsorption on Au(100) have shown a variety of sulfur organizations on this substrate [47–49, 52]. The easiest formed one is the p(2×2)-S phase, which has an interatomic distance of 5.6 to 5.8 Å (2x the Au-Au distance) with a S coverage of 0.25ML and it is modeled as a S atom adsorbed on alternating four-fold hollow sites. It was imaged from experiments with S_2 dosing with electrochemical source [47, 49] and S dosing with alkaline solutions [48, 52], with both STM measurements at Room Temperature and Low-temperature. A higher sulfur dosage transforms the p(2×2) surface into a (2×2) pattern with a higher density of S atoms, called a trimer phase. *Jiang et al.* [47] reported this structure as an intermediate phase between the transition from p(2×2) phase to c(2×4) phase. This trimer phase consists of a S_3 compound placed in the four-fold hollow site of the Au surface. As the sulfur dosing increased, the surface turned into c(2×4) pattern, showing 5 S atoms on the four-fold hollow sites with a S_3 trimer compound on top of a S_2 compound. The authors [47] indicated that for annealing the sample at temperatures higher than 380K, this pattern was lifted, which indicates that for experiments of sulfur adsorption from sources that need post-annealing (as H_2S and SO_2) might not be possible to obtain this c(2×4) phase. LEED measurements showed that a sharp c(2×4) phase can be obtained by saturation of a highly ordered (2×2) phase, which comes from post-annealing a rough c(2×4) surface.

Studies of adsorption of sulfide species from alkaline solutions [48, 52] indicated two different structures defined as c(2×6) phase and dimer complexes. The c(2×4) phase appears as zigzag chains with distance of 5.7 Å between chains and S-S distance within a single chain of 4.07 Å, while the dimer complexes coexist with other S structures as the p(2×2) and c(2×4). *Schlaup and Wandelt* [48] suggested that these dimers were composed of both Au and S atoms due to the change of the step morphology when these particles were formed, leading to kinked steps.

The authors also found this dimers to have an apparent height of 1.4 Å above the zigzag chains and a distance between adjacent maxima of 5.8 Å.

A last feature found in most of the studies in the literature was a square-like shaped gold sulfide compound. This structure was found both on Au(100) [48, 52] and Au(111) [46], in UHV driven experiments and also under electrochemical conditions. While *Maza et al.* [52] reported a 5.0 Å length, *Schlaup and Wandelt* [48] described it as 8.5Å. A proposed model by *Maza et al.* [52] suggests that this structure is formed by 8 S atoms organized in S_2 dimers and coordinated around a central Au adatom, which originates from the lifting of the Au(100) reconstruction at even small coverages. All dimers are expected to adsorb-on-top sites and each one has a sulfur atom bond to the central Au atom. This square-shaped feature has an apparent height of 0.6 Å compared to the (2×2) phase with which they coexist.

Low temperature STM measurements made by *Walen et al.* [49] displayed a variety of Au-S complexes with diamond-shaped (Au_4S_5), incomplete diamond-shaped (Au_3S_4, Au_2S_3), or oblong-shaped (AuS_2) structures, which were only visible due to immobilization of sulfur adsorbed species generated by the 5K temperature. Room Temperature STM measurements suggest that the high sulfur diffusion signature lies as streaky noises in the scanned images.

3.3 CoO_x/Au(111)

Noble metal oxides are known for their high catalytic activity toward the Oxygen Evolution Reaction (OER) [53, 54], which is responsible for the oxidation of water in the production of molecular hydrogen. However, the high cost and limited availability of these materials motivate the search for more abundant and economically viable alternatives. Among the materials investigated for this purpose, cobalt oxides have been studied on a variety of metallic substrates, including Ir [55–57], Au [58–61], Pt [57, 58, 61, 62], and Ag [58, 63]. Since Au(100) was used as the substrate in the present work, the literature review was focused on studies involving Au substrates that are most relevant to the results and discussion presented in this thesis. In particular, cobalt oxide in its spinel Co_3O_4 structure exhibits significant catalytic activity toward the water oxidation reaction, and recent studies have shown that the Au/cobalt oxide interface can significantly enhance the catalytic activity of this compound [64].

STM studies of the growth of cobalt oxide on Au(111) [60, 61, 64] have found three different adsorption structures: (1) a bilayer of -Co-O, (2) trilayer composed of -O-Co-O, and (3) a multilayer structure of -O-Co-O-Co-O, defined as a bilayer

grown on top of a trilayer structure. The first one appears as single and double layers and it is obtained by evaporating cobalt in low oxygen pressure (typically $1.0 \cdot 10^{-6}$ mbar O_2), while the two other structures can be obtained with higher oxygen pressures (greater than $1.0 \cdot 10^{-5}$ mbar O_2). *Fester et al.* [61] indicated a dependence between the structure formed and the temperature of post-annealing at elevated oxygen pressure, where for annealing temperatures above 573K, exclusively multilayers islands were present. DFT calculations have shown that the single and double layer Co-O bilayers are the most stable configuration at low oxygen pressure with cobalt showing hollow sites as the preferential adsorption sites. Meanwhile the O-Co-O trilayer is the most stable configuration at high oxygen pressures, where the oxygen terminated films prefer to adsorb on top of the Au surface atoms [64].

The bilayer and double bilayer show a 5-10nm wide hexagonal truncated shape with an hexagonal moiré pattern on top. The apparent heights and moiré pattern periodicity being 1.6-1.9 Å and 37Å for the single bilayer, and 4.0 Å and 31Å for the double layer, while for both islands the interatomic distance was found to be 3.3 Å. *Fester et al.*[61] interpret these islands as rocksalt CoO(111) and wurtzite CoO(111), respectively, although the slight difference between the interatomic spacing and apparent height from the previously reported CoO(111) (3.02 Å and 2.46 Å). Single layer Co-O STM images in the literature indicate the appearance of bright line features defined as excess adsorbed oxygen, as an intermediate stage between the bilayer and the trilayer formation.

For the trilayer structure, the apparent height found in the literature is between 2.7 Å and 3.0 Å and the same interatomic spacing as the bilayer islands. This information led *Fester et al.* [61] to conclude that trilayer structures are CoO(111) compound with rocksalt organization, where the greater oxygen pressure forces the incorporation of a layer of oxygen atoms between the Au substrate surface and the first cobalt layer. This changes the oxidation state of cobalt (from Co^{+2} to Co^{+3}) without damaging the structure of the islands. Some studies indicate the presence of structures on top of these islands interpreted as OH group formation due to the trilayer's water splitting properties even in very low pressures of H_2O present. *Diekhöner et al.* [59] indicated that the trilayer islands showed a more metallic behavior, suggesting this structure as the one with higher catalytic activity, while the multilayer was seen to have a more insulating nature. Some articles have defined these islands with the same hexagonal truncated form as the bilayer ones, though other describe them as having no clear symmetry.

Lastly, the multilayer structures have apparent height of 4.6-5.0 Å and, as mentioned above, are described as Co-O bilayer islands grown over O-Co-O tri-

layer structures. Since it is a composition of the previous two analyzed structures, the cobalt oxidation states present are Co^{+2} and Co^{+3}.

To the best of our knowledge, no studies on cobalt oxide on Au(100) had been reported in the literature prior to this work.

3.4 CoS_x/Au(111)

Transition Metal Dichalcogenides (TMDs) consist of a layer of transition metal atoms positioned between two layers of chalcogen atoms (S, Se, or Te). This class of materials has been extensively studied over the past decades due to its wide range of potential applications, including optoelectronics, such as counter-electrodes for solar cells [4], high-density data storage [1–3], efficient energy harvesting, including artificial photosynthesis [7, 8], and catalysis [11, 12]. Gold substrates are commonly employed for the growth of single-layer TMDs, as their high affinity for chalcogen atoms is believed to contribute to the stabilization of these structures. Regarding cobalt sulfide, studies have reported its growth on non-crystalline substrates, such as glass [65] and silicon [66], as well as on Au [67, 68] and Ag [69] single crystals. In addition, cobalt sulfide nanostructures have been extensively investigated [6, 14, 16]. Considering the greater relevance to the present work, this literature review focuses primarily on studies of cobalt sulfide growth on Au(111).

STM studies of the growth of cobalt sulfide over Au(111) indicated that the sulfurization of cobalt has a very low energy barrier with cobalt nanoparticles being extremely unstable in even mildly sulphiding environments and sulfurizing at Room Temperature (RT) [67]. Two main pathways for obtaining cobalt sulfide are found in the literature: 1) evaporating cobalt over a substrate and then exposing it to a sufur-rich atmosphere of gaseous H_2S and 2) evaporating cobalt in a sulfur-rich atmosphere of gaseous H_2S.

Kibsgaard et al. [67] took the first approach in its work published in 2008. The authors evaporated cobalt on a Au(111) single crystal and exposed it to a mild sulphiding environment ($5.0 \cdot 10^{-8}$ mbar) for 80 hours, maintaining the sample at RT. The results showed that the cobalt agglomerates converted into Co_3S_4 complexes with characteristic dimensions of 20 ± 2 Å or integer multiples thereof. The Co_3S_4 complexes formed in the perimeters of the metallic islands and diffused rapidly agglomerating in a cobalt sulfide phase, which, together with an analysis of time evolution, indicated that the sulfur induced corrosion depends on the number of available sites on the perimeter of the nanoparticles. Three layer cobalt nanoparticles showed a lower decay rate when compared to double-layer

cobalt nanoparticles, suggesting that the saturation of sites at the rim hindered sulfur from accessing the remaining metallic cobalt in the middle of the particles. The model proposed by the authors indicated that H_2S initially physisorbs on the Au(111) surface and then diffuses to the cobalt nanoparticles, mainly interacting at the interface between the gold substrate and the cobalt nanoparticles. Through the low temperature STM images, the physisorbed H_2S was found to appear as a striped phase and the Co_3S_4 islands were found to show a Moiré pattern due to the lattice mismatch between the non-rotated overlayer, 3.4 ± 0.1 Å, and the substrate, 2.95 Å, defined as a "mill-wheel" pattern. These islands appeared with an apparent height of 2.60 Å and interatomic distances that matched the S-S distance in the $Co_3S_4(111)$ surface. Using a Auger Photoelectron Spectroscope [67], the Co:S ratio was found to be approximately 8:3, attributed to a stacking of $S_4 - Co_3S_4 - S_4$. By heating the cobalt sulfide sample to 523K in the same H_2S atmosphere, larger sheets of homogeneous Co_3S_4 were obtained.

A more recent work from *Prabhu et al.* [68] obtained a different phase of cobalt sulfide by choosing the second approach described above. 2D CoS(0001)-like sheets were grown on Au(111) through the evaporation of cobalt in a $2.0 \cdot 10^{-6}$ mbar atmosphere of H_2S, maintaining the sample at 410K, and a post-annealing for 20 minutes at 650K in the same atmosphere. These sheets showed a hexagonal structure in its basal plane that consisted of a rhombus-shaped unit cell with side length of 1.97 nm (7 Au-Au distances) and an apparent height of 2.43 Å. Six bright spots appeared along the rhombus-like unit cell edge with distance between adjacent spots of 3.3 Å. Although interatomic distance found by *Kibsgaard et al.* [67] and *Prabhu et al.* [68] seemed similar, the Co:S ratio obtained by *Prabhu et al.* with X-ray Photoelectron Spectroscopy was 1:2.09, indicating a $S - Co - S$ stacking of the CoS(0001)-like sheet. In order to distinguish between a Co_3S_4 and a CoS phase, Density Functional Theory (DFT) calculations were used and the corresponding STM image simulations were generated. The authors tested the relaxation of both cobalt sulfide phases considering the influence of the Au substrate and found that the CoS(0001) phase showed similarity to the experimental results already mentioned here. Due to the lattice mismatch between cobalt sulfide and the substrate, cobalt sulfide exhibited a Moiré pattern with a maximum apparent height variation of 0.5 Å. The authors pointed out a metallic behavior exhibited by the cobalt sulfide sheets, contrary to most TMDs, due to the sulfur interaction with gold.

To the best of our knowledge, no studies on cobalt sulfide on Au(100) had been reported in the literature prior to this work.

Chapter 4

Materials and Methods

4.1 UHV system

Under ambient conditions, surfaces are continuously exposed to atmospheric gases, liquids, and particulate contaminants, which readily adsorb onto them. For surface science investigations, the presence of these unwanted species can obscure the intrinsic properties of the surface of interest and interfere with experimental measurements. Consequently, most surface science experiments are performed under ultra-high vacuum (UHV) conditions to minimize surface contamination and ensure well-defined and reproducible surfaces. In this system, we work with a model surface to investigate the interaction of the chosen sample with the desired material, aiming to diminish most of the possible sources of contamination.

The UHV system contains many components, such as vacuum pumps, vacuum gauges, vacuum chambers and valves. The vacuum categories are classified as a function of the pressure range: going from 10^{3} mbar to 10^{-10} mbar [Figure 4.1].

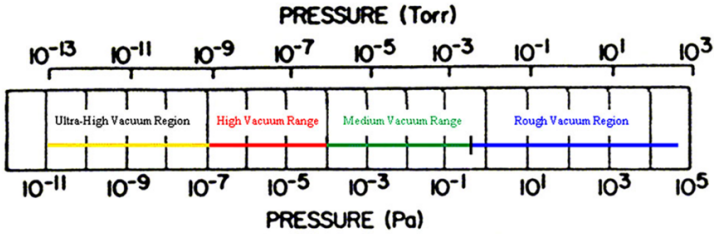

Figure 4.1: *Vacuum categories and pressure ranges [70]*

For each range of pressure, a distinct type of pump and gauge is used. Figure 4.2 shows the pressure range of the most common types of pumps and gauges.

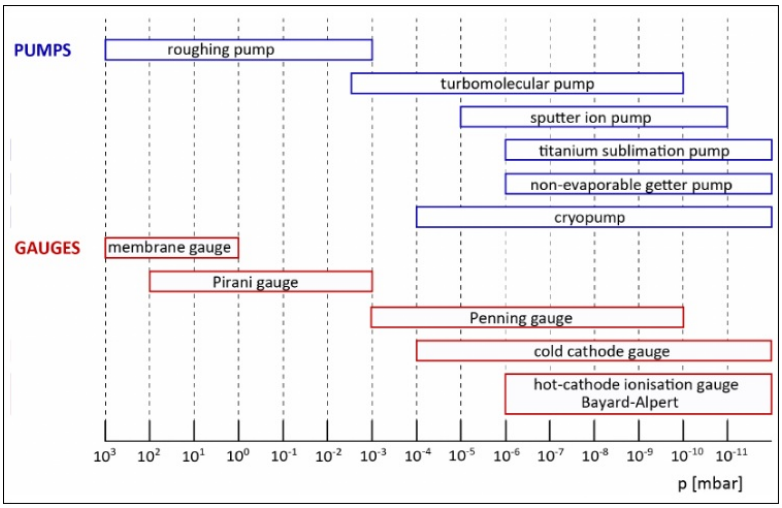

Figure 4.2: *Work pressure for different types of gauges and pumps. Illustration from [71].*

4.2 Experimental Setup

The experiments were conducted in two separate UHV systems, one equipped with the STM and the other with the XPS system.

4.2.1 STM vacuum system

The STM experimental setup consists of three vacuum chambers separated by valves, each having a turbomolecular pump coupled to it. The sample is introduced into vacuum through the loadlock by the removal of its window. This introductory chamber gives access to the sulfidation chamber in one side and the main chamber on the other.

The load-lock is the entry to all the samples in this system. This vacuum system features a turbomolecular pump connected to a mechanical oil pump, cold cathode gauge, and two gate valves, one separating the load-lock from the main chamber and the second one separating the load-lock from the sulfidation chamber. The load-lock is connected to both the main chamber and the sulfidation chamber, serving as a transfer chamber between them and minimizing the risk of exposing the STM to the highly corrosive H_2S gas.

The sulfidation chamber features a turbomolecular pump connected to an additional mechanical oil pump, hot cathode ionization gauge, and a leak valve to insert gas into it. All experiments with gaseous H_2S take place here.

The Scanning Tunneling Microscope is located in the so-called "main chamber", which also features two evaporators, two ion guns (one for sample cleaning and the second one for tip cleaning), a cold cathode gauge, a hot cathode ionization

gauge, two leak valves for gas insertion (each one connected to an ion gun), a turbomolecular pump connected to a mechanical oil pump, a sputter ion pump, and a titanium sublimation pump.

Linked to each leak valve, there is a piping system, used to transport gases from the cylinders to the desired chamber. For the highly corrosive H_2S gas there is a separate gas line, while the remaining gases share a common gas line connected to the leak valve. Each gas is supplied through a dedicated line from the cylinder to the gas manifold. A common practice to ensure the lowest contamination is purging the piping system three to five times with the gas to be used in the subsequent experiment. For that, a mechanical oil pump is coupled to the tubes. To avoid contamination, the H_2S tube has a dedicated pump.

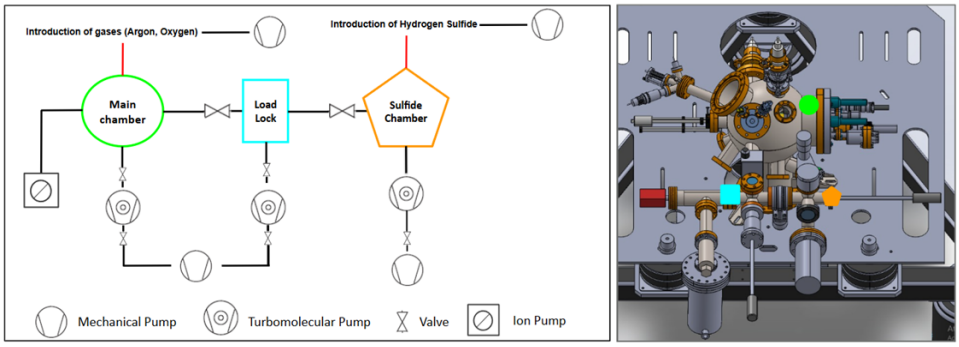

Figure 4.3: *Experimental Setup showing the different UHV chambers, valves and pumps, on the left, and a Solid Works scheme, on the right.*

4.2.2 XPS vacuum system

The XPS experimental setup is not directly connected to the STM system. It consists of five chambers interconnected by a vacuum transfer line equipped with a sample transfer mechanism, allowing samples to be moved between chambers without breaking the vacuum. This vacuum system comprises a preparation chamber, a high-pressure sulfidation chamber, a load-lock chamber, the XPS analysis chamber, and an IRRAS (Infrared ReflectionAbsorption Spectroscopy) chamber, where measurements are performed using a Fourier-transform infrared (FTIR) spectrometer. Each chamber is connected to a turbo-molecular pump attached to a roughing pump, including the vacuum tubes for handling the samples, and gauges to control their vacuum pressures.

The load-lock works similarly to the previously described one. The samples enter the system through this chamber. The preparation chamber features an ion gun and a heating system by electron bombardment for sample cleaning, three e-beams evaporators - one of them used in this work to evaporate cobalt, two

leak valves for the insertion of gases into the chamber (which allow oxidation, for example), and a Low Energy Electron Diffraction apparatus. The high-pressure sulfidation chamber features a ceramic heating system and a leak valve for the insertion of gaseous H_2S on the chamber. The IRRAS chamber features a leak valve for gas insertion, an ion gun and a heating system by electron bombardment for sample cleaning.

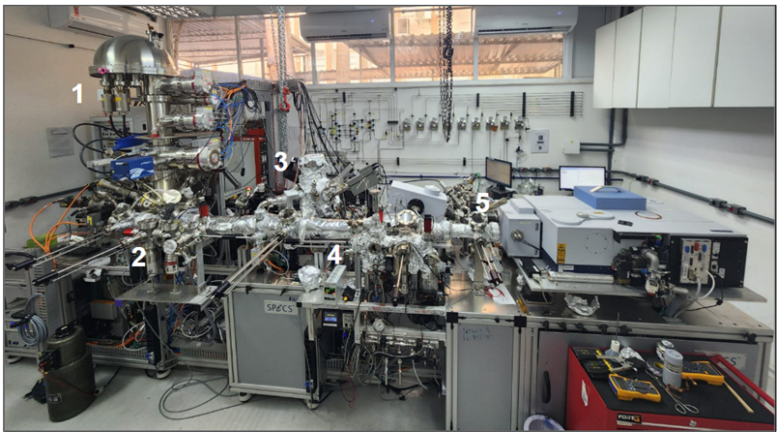

Figure 4.4: *Vacuum system composed of: (1) X-ray Photoelectron Spectroscope, (2) Loadlock chamber, (3) Preparation Chamber, (4) Sulfidation Chamber and (5) FTIR-IRRAS.*

The XPS instrument consists of three main components: the analysis chamber, where the sample and the X-ray source are located; a column of electrostatic lenses that guides the emitted photoelectrons to the electron energy analyzer; and the electron energy analyzer, which houses the detector. Since this specific apparatus can measure Near Ambient Pressure (NAP), it is coupled with a series of turbo-molecular pumps to enable differential pumping.

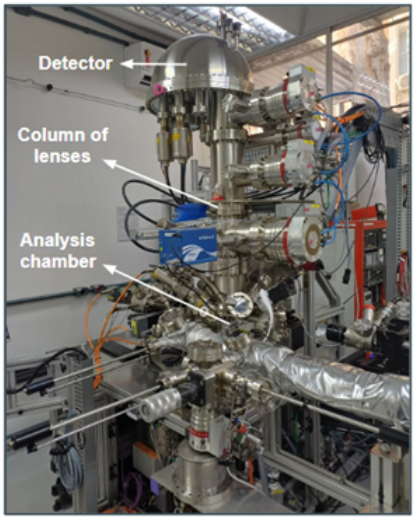

Figure 4.5: *Photo of the XPS from the Interface Lab in CBPF with highlights.*

4.3 Sample preparation

Samples in UHV are typically prepared by cycles of sputtering (mechanical ion bombardment) and annealing (electron bombardment heating). The first step consists of filling the preparation chamber with Argon gas and then using an electric field to ionize the gas and accelerate the generated ions in the target direction, physically interacting with the sample by momentum transfer from the ion to the surface atoms. This step is crucial for the removal of adventitious carbon, created by the interaction between the sample surface and air, and/or surface contaminants, yet the energetic ions will interact with all atoms on the surface, which may result in the removal of atoms from the sample. The second step, the annealing process, consists of accelerating electrons toward the sample holder by electron emission from a filament through the Joule effect and directing them by a high voltage applied between the sample holder and the filament. The electrons then hit the sample holder, heating the sample by transferring their energy and allowing the surface atoms to reorganize into the most energetically favorable configuration.

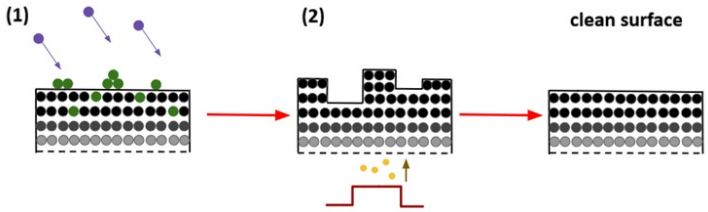

Figure 4.6: *Scheme of sample cleaning under UHV conditions: (1) ion sputtering and (2) annealing. Green circles represent contaminant atoms, purple circles represent argon ions, black circles represent the atoms at the sample surface, gray circles represent atoms in the bulk, and yellow circles represent electrons thermionically emitted from the filament. Author's own illustration.*

A clean Au(100) surface was obtained by repeated sputtering and annealing cycles. Sputtering was performed using 1 keV Ar^+ ions for 30 min, followed by annealing at 823 K for 30 minutes and a subsequent 10 seconds flash annealing at 973 K repeated three times, after which the sample was cooled under a controlled cooling ramp.

4.3.1 Evaporation of cobalt on Au(100)

Cobalt was evaporated onto the Au(100) single crystal using a commercial EFM 3 Omicron UHV Evaporator. The clean Au(100) sample was maintained in the microscope during the degas and stabilization of the evaporator. In order to do

that, first the water cooling was turned on, followed by the high voltage and then the gradual increase of the filament current. When the evaporation flux reached approximately 5.0 nA, the evaporant and the other components of the evaporator were degassed for 5 min. The flux was then reduced to 2.0 nA and maintained at this value for an additional 5 min to stabilize the evaporation process. Since the evaporation can only occur with the valve between the load-lock and the main chamber open, this valve was opened simultaneously with the initialization of the evaporator (about 10 minutes to stabilize the pressure between the chambers). Lastly, the sample was transferred to the wobble stick, placed in position, and evaporation was started.

To study the nucleation and initial stages of the interaction of cobalt evaporated on the Au(100) surface, first a flux rate was chosen based on the analysis of STM images and evaporation rate estimation in ML/min. The parameters of the e-beam evaporator were: filament current at 2.5A, high voltage at 950V, emission current set to 18.2mA and a flux of 2.0 μA. The time of evaporation was varied from 30 seconds to 10 minutes, with post-annealing the last sample in order to analyze the cobalt diffusion inside the gold substrate.

4.3.2 Sulfurized Au(100)

The clean surface of Au(100) was exposed to H_2S and maintained at different temperatures for the same period of time in a separate chamber, determined in this work as the sulfidation chamber. The sample was transferred from the main chamber to the sulfidation chamber via the load-lock chamber. The crystal remained in the Microscope while the valve-opening sequence was carefully executed to minimize contamination of the surface. In all experiments performed in the sulfidation chamber, the pressure was maintained between 1.0 and 2.0 10^{-5}mbar, the sulfurization time was 15 or 30 minutes and the temperature of the sample varied from 300K to 723K.

4.3.3 Growth of cobalt oxide on Au(100)

The cobalt oxide film was grown by the evaporation of cobalt in an atmosphere of molecular oxygen. The same process of stabilizing and degassing the evaporator described in the previous section was applied here, but carried out in a O_2 atmosphere, while the load-lock-main chamber valve was maintained open.

The oxygen pressure was kept at 5.0 10^{-7} mbar or $1.0 \cdot 10^{-6}$mbar while the evaporation took place and then the sample was post-annealed with an emission

current of 1.0 mA for 15 to 25 minutes.

4.3.4 Sulfurization of CoOx

All sulfurization experiments were carried out under an H_2S pressure of 1.0×10^{-5} mbar. In each experiment, the sample temperature was kept constant, with separate experiments performed at temperatures between 343 K and 573 K.

4.4 Scanning Tunneling Microscopy - STM

Scanning Tunneling Microscopy is a type of Scanning Probe Microscopy (together with the Atomic Force Microscopy, the Scanning Probe Electrochemistry, the Near-Field Scanning Optical Microscopy and many others) that allows the study of surfaces at the atomic level, with size images ranging from 1 Å to 1 μm. This technique was invented by Gerd Binnig and Heinrich Rohrer [72] in 1981 and resulted in the award of a Nobel Prize in Physics in 1986 .

4.4.1 Operation

The Scanning Tunneling Microscope generates an image by scanning the surface of a sample with a sharp tip and detecting the tunneling current arising from the tipsample interaction. The current is amplified through a pre-amplifier allowing the measured picoampere (10^{-12}) value to be enhanced to microampere (10^{-6}). From this electrical signal, the software produces a figure showing dark and bright patterns. An additional important part of the Scanning Probe Microscopy is the application of a feedback system, which means the software is constantly sending feedback to itself to ensure a better result.

Three requirements must be fulfilled for a sample to be measured in the STM: the sample must conduct electricity well, the material of the tip must be conductive and the surface of the sample must be relatively flat (with its roughness having a maximum height of dozens of nanometers). These prerequisites arise from the images being made by the tunneling current of electrons and the atomic scale of the microscope.

The Scanning Tunneling Microscope has two types of movements: the movement of the motor head (where the tip is mounted) and the scanning of the tip. When a sample is inserted in the STM, the distance between the tip and the sample surface must be long enough to avoid breaking the first one and damaging the flat and conductive sample. Starting the measurements, the tip is brought close

to the sample by a set of 3 piezoelectric actuators connected to a shaft in a movement called inch-worm, because it resembles the way a worm moves. Its system begins in a state of relaxation of the piezoelectric ceramics and it moves in a cycle of 6 steps: (A) The upper piezo relaxes, while the lower piezo is electrified and clamped to the shaft; (B) The center piezo is electrified and extends to the direction of movement; (C) The upper piezo is electrified, clamping to the shaft; (D) The lower piezo relaxes; (E) The center piezo relaxes, bringing the lower piezo closer to the upper piezo; (F) The lower piezo is electrified, clamping to the shaft. Each time the piezoelectric system completes this set of movements, the STM software counts a step in the motor control unit.

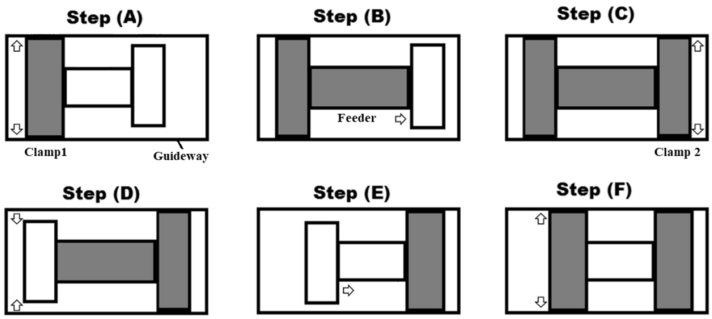

Figure 4.7: *The inch-worm movement explanation [73]*

The second movement of the STM is scanning the surface. This is possible due to an extremely narrow conductive tip, usually made of W or a composition of Pt/Ir. In order to allow the scanning movement, the tip is mounted over a sectioned piezoelectric system, where when a certain voltage is applied, the piezoelectric ceramics deform and the tip is moved. This piezoelectric system consists of five sections, four of which control the tip-movement in the x and y directions and the last one controls the movement in the z-direction (perpendicular to the sample surface).

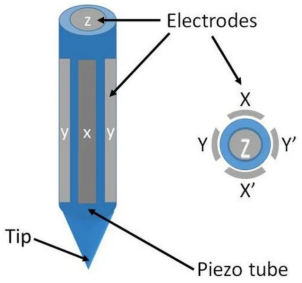

Figure 4.8: *Piezoeletric sections in the STM tip*

There are two modes of acquiring an image with the STM: the constant current mode and the constant height mode. In the first one, the user sets a current

and while the tip is scanning the sample, it will vary its distance from the sample when encountering a higher or smaller structure. When using the constant current mode, the system is continuously acquiring the tunneling current value, comparing with the value set by the user and correcting the sample-tip distance based on that value, ensuring the most accurate parameters. This mode is applied for studies where one expects a surface roughness. In the second mode, the user sets a z value (distance from the sample) and the microscope generates an image based on the variation of the tunneling current. It is only used for samples known to be extremely flat due to the risk of crashing the tip. Due to the exponential dependence of the tunneling current on the tip-sample distance, STM is highly sensitive to mechanical vibrations and environmental noise. The SPECS Aarhus 150 used in this work employs a spring suspension system to damp external vibrations and reduce mechanical noise during STM measurements. In this system, the STM was mounted on a system of pneumatic stabilizers to enhance the image stability.

4.4.2 STM Calibration

A gold single crystal with facet (100) was chosen as the substrate for the cobalt sulfide film. Due to its inert character in most chemical reactions and its extensive characterization in the literature, gold was selected as a substrate for the growth of the thin film, allowing the investigation of its structural and electronic properties. This transition metal has a face centered cubic (FCC) unit cell in its bulk configuration (Figure 4.9).

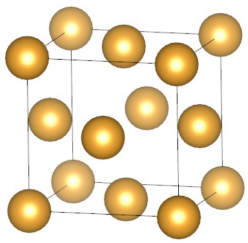

Figure 4.9: *Unit cell of bulk Au generated using VESTA. [17]*

This particular facet has a reconstruction called *quasi-hexagonal*, for which different authors have described distinct unit cells, for example c(28×48) [74] and (5×20) [75]. This reconstruction presents a Moiré pattern in the latest atomic layer that appears as stripe-like figures. The stripes consist of seven rows of atoms and come from the relaxation of the latest atomic layers of the gold crystal, where the atoms in the bulk have a square-like symmetry and the surface organizes with

hexagonal symmetry (Figure 4.10), resulting in a modulation of the atoms in the surface (Figure 4.10) with apparent maximum height of 40-60 pm.

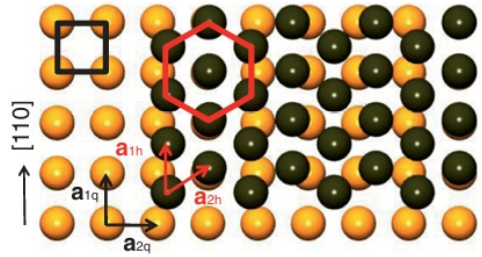

Figure 4.10: *Structural mismatch between the hex top layer and the square bulk symmetry (atoms in black are the ones at the surface and atoms in yellow are the ones in the bulk). Illustration from [74].*

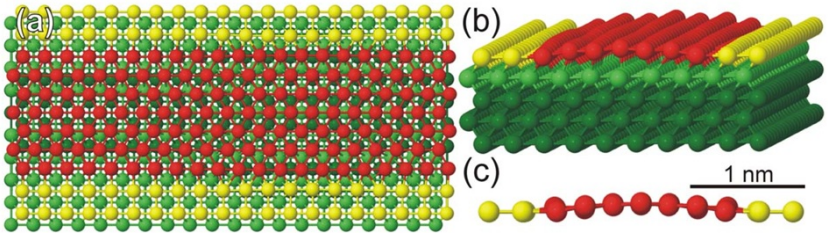

Figure 4.11: *Moiré Pattern from Au(100) surface which appears after relaxation (green atoms are the ones in the bulk, yellow atoms represents atoms with a square symmetry and red atoms are the one with a hexagonal symmetry). Illustration from [75].*

The distance between the stripes and the step height of the facet (100) were analyzed to calibrate the data analysis from STM images presented in the next chapter, which based on literature are 1.44nm and 0.204nm, respectively ([76]).

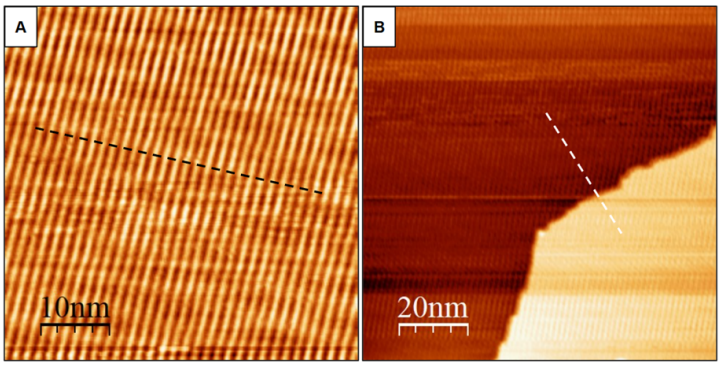

Figure 4.12: *STM images used as references for calibrating distance measurements using the WSxM image processing software: (A) Au(100) reconstruction with distance between stripes of 14.4 Å (image size: 50 nm x 50nm, Bias = 1000mV and I = 800pA) and (B) One monoatomic step of Au with height of 2.04 Å (image size: 100nm x 100nm, Bias = 1000mV and I = 800pA).*

Image calibration was carried out through the clean gold surface of Au(100) with images featuring its characteristic reconstruction and a monoatomic step of gold. For each clean Au(100) measurement, one image with a step and one image

with the characteristic stripes was chosen. Then the step height and the distance between adjacent stripes were obtained and corrected according to the literature values.

4.5 E-beam evaporator

4.5.1 Operation

In a commercial evaporator, the filament current or the emission current can be controlled by its user. By setting a filament/emission current high enough to generate a flux of material, the evaporant will start to exit by the evaporator aperture. After the aperture, there is a shutter, responsible for preventing the material from exiting the evaporator. Right before the aperture, some commercial evaporators (including the one used in this work) have a module dedicated to measure the flux rate. Inside this module there is a filament responsible for emitting electrons by the thermionic effect. When the emitted electrons collide with some of the evaporated material (that has to cross this module to exit the evaporator), it ionizes and these ions are collected by a detector using an electric field. In the results section, these parameters will be informed for all experiments.

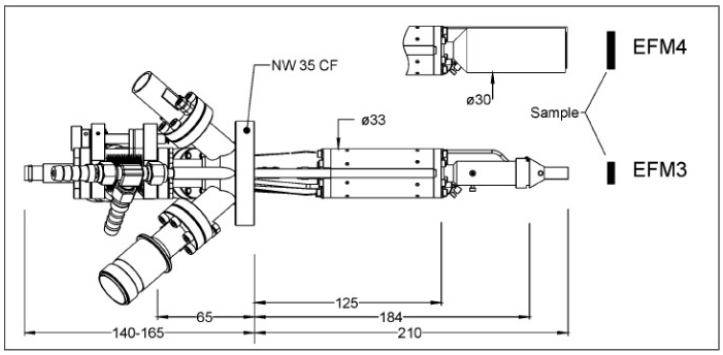

Figure 4.13: *Illustration of the EFM3i evaporator used in the present work from the Omicron user manual.*

4.5.2 Coverage calibration

To calibrate the rate of Monolayer per minute, the first two experiments were made with a low flux rate and a high flux rate, respectively. Based on them the best flux rate was chosen and applied for all the following experiments. To study the nucleation and first steps of the evaporation of cobalt on Au(100).

The rate of ML/min was obtained by analyzing an image of cobalt evaporation for 2 minutes, measuring the height of the islands, their area and comparing this

information with the theoretical value of one step height of hcp Co. The resulting value was approximately 0.38ML/min.

4.6 Sulfidation Chamber

4.6.1 Operation

The sulfidation chamber is a small chamber with a wobble stick to transfer the samples and a manipulator, with a small tube in a U-shape at its apex to ensure high pressures in the sample region and a heating system. The heating is achieved using a ceramic component with a filament inside, in which current or voltage is controlled by its user. The high temperatures, homogeneous heating, and strong resistance to corrosive atmospheres are the main distinguishing features of this heating method. Since this work was based on the exposure of a sample to a highly corrosive atmosphere of hydrogen sulfidation, the heating inside this atmosphere could not be hindered by the gas itself.

Ceramic is an electrical insulating material capable of enduring high temperatures while presenting little to no deformation or out-gassing of materials. When a tungsten or molybdenum filament is mounted inside a ceramics pot or tube, the Joule Effect caused by an electrical current flowing through the filament heats the ceramics. If a sample holder is placed in contact with the heated ceramics, while electrically insulating the sample from the filament, it results in the heating of the sample by conduction and radiation.

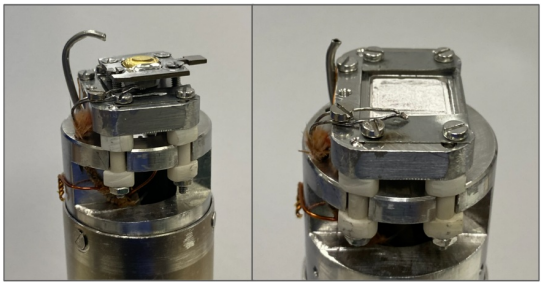

Figure 4.14: *Photo of the sulfidation chamber manipulator.*

4.6.2 Temperature Calibration

The temperature calibration of the sulfidation chamber was performed through comparison between two closely placed thermocouples. The permanent one is a type J thermocouple placed in a screw in the manipulator close to the sample

holder, while a sample holder with a type K thermocouple attached to it was inserted in the chamber.

Each temperature was maintained for 30 to 45 minutes during the heating ramp and for 5 minutes for the cooling ramp. Figure 4.15 shows the resulting correlation. An increasing discrepancy between the two temperatures was observed with increasing filament current. Therefore, all temperatures reported in this thesis were corrected using this calibration procedure.

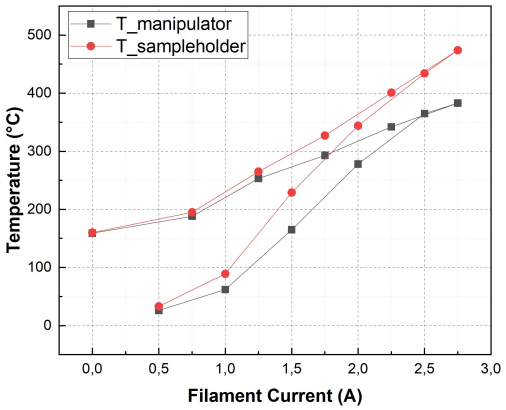

Figure 4.15: *Temperature versus current in the filament - Temperature calibration of the sulfidation chamber. Authorial production.*

Since the ceramic component of this setup has a resistance of 2.1 Ω, a graph relating the temperature to the power dissipated by the ceramic heater was produced.

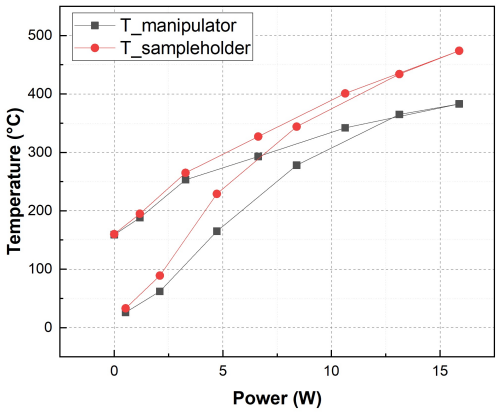

Figure 4.16: *Temperature versus power - Temperature calibration of the sulfidation chamber. Authorial production.*

4.7 X-ray Photoelectron Spectroscopy - XPS

4.7.1 Operation

The operation of an XPS consists of an X-ray source that irradiates soft X-rays over a sample causing the emission of photoelectrons which are then collimated and retarded by the electromagnetic lenses until they reach the detector (Fig. 4.17). The X-ray source from the SPECS PHIBOS150 XPS present in the Interface Lab at the CBPF is a Monochromatic Al K_α that irradiates photons with energy of 1486.7eV by bombarding an aluminum anode with high-energy electrons. The photoelectrons emitted by the interaction with these X-rays are collected and retarded by the system of electromagnetic lenses before reaching the detector. The count of electrons per time unit as a function of the electron energy produces an XPS spectrum of intensity (in arbitrary units) per energy (in eV). In the next paragraph the detector will be explained in detail.

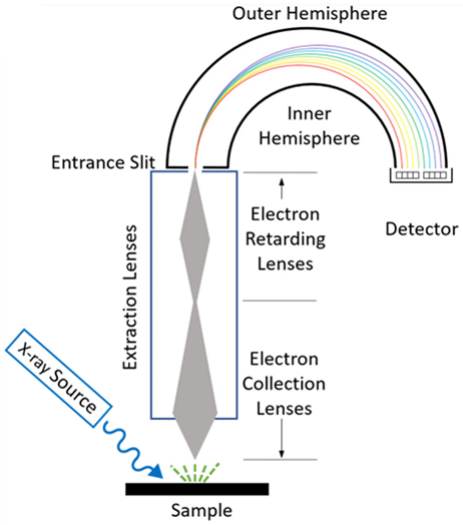

Figure 4.17: *Scheme of an X-ray Photoelectron Spectroscope adapted from [29].*

The analyzer present in this system is a hemispherical analyzer composed of two concentric hemispheres with radius R_{in} and R_{out}. When the electron emitted by the sample passes through the extracting lenses system, it is directed to the entrance slit of the analyzer with energy E_i and it is slowed by a potential difference $\Delta V = V_{in} - V_{out}$ before reaching the detector, such that [77]

$$E_i - e\Delta V = E_0. \tag{4.1}$$

E_0 is called the pass energy and it is defined as the energy needed by an electron to cross from the entrance slit of the analyzer to the detector along the equipotential plane described by the medium radius R_0, as depicted in Fig. 4.18. This potential

difference must satisfy the relation [77]

$$e\Delta V = E_0 \left(\frac{R_{out}}{R_{in}} - \frac{R_{in}}{R_{out}} \right). \tag{4.2}$$

The potentials of both hemispheres are set according to the pass energy E_0, which is closely related to the energy resolution of the spectrum ΔE. Typically, $\frac{\Delta E}{E_0}$ remains constant, at approximately $\sim$2% of the resolution. Consequently, if the pass energy is high, the resolution of the spectrum will be low and vice-versa.

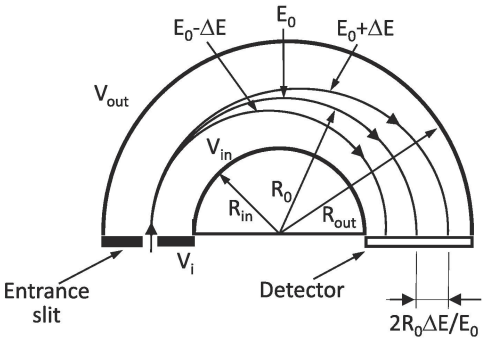

Figure 4.18: *Scheme of the hemispherical analyzer adapted from [78]*

Chapter 5

Results and Discussion

Most studies reported in the literature use Au(111) as a substrate, because the formation of highly ordered overlayers on Au(100) is hindered by its complex surface reconstruction. However, gold nanoparticles and nanostructures used in applications such as medicine and chemical sensing commonly contain a significant fraction of {100} facets, motivating further investigation of this surface orientation. In this context, understanding the interaction of each precursor species with the Au(100) surface is essential for elucidating the mechanisms governing cobalt sulfide growth and for the reliable interpretation of the resulting STM data.

For the correct interpretation of STM images acquired after cobalt sulfide growth, two crucial preliminary studies were conducted: 1. metallic cobalt was deposited onto the clean substrate, and 2. after restoring the clean surface, the bare substrate was sulfurized. These two groups of experiments were designed to investigate the individual interactions between Au(100) and each precursor species, Co and H_2S. As will be shown throughout this chapter, these experiments proved essential for the analysis of the STM data, enabling the identification of features containing only Co and Au, as well as AuS complexes formed during the sulfurization of metallic cobalt particles or cobalt oxide structures.

5.1 Adsorption and growth of cobalt on Au(100)

In order to study the nucleation and initial stages of cobalt growth on an Au(100) surface a series of experiments were conducted by varying the evaporation time while maintaining the rest of the parameters fixed.

After 30 seconds of evaporation, it was observed that cobalt ad-atoms nucleated on top of the highest gold atoms of the Au(100) reconstruction as shown the inset of Figure 5.1, which are approximately 60 pm higher than the lowest atoms of the surface reconstruction, as previously mentioned. The apparent heights of

the islands on Figure 5.1 were 1.43 Å or 3.05 Å, which are attributed to one monolayer and one bilayer of bcc-Co islands, respectively. Co-evaporation studies with Au(111) reported the tendency of some metals to nucleate at the elbow of the characteristic herringbone reconstruction due to a lower kinetic barrier for place exchange at these sites [79]. Thus, since cobalt is one of the metals that nucleate at these specific sites, the nucleation site of metallic Co for Au(100) may indicate where the mechanism of place exchange is more favorable on this surface.

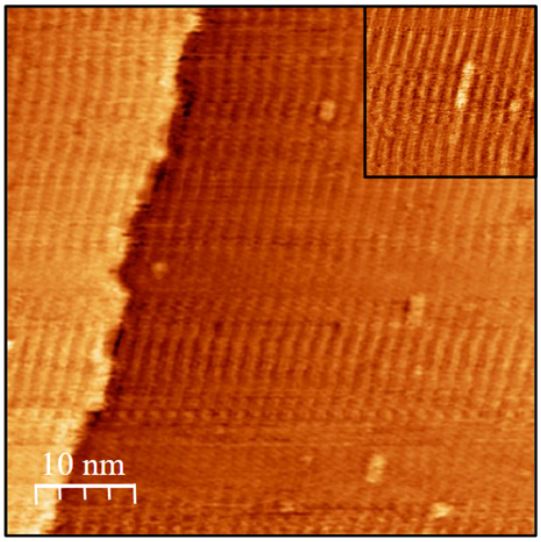

Figure 5.1: *STM image showing the nucleation of cobalt atoms. Inset size: 20 nm x 20 nm. Both images with the same scanning parameters: Bias=1600mV and I= 700pA.*

As the evaporation time increases, the cobalt islands become rectangular with the longer sides parallel to the <011> direction of the Au(100) surface. It is noticeable from the following images that the cobalt islands complete an integer number of stripes of the gold reconstruction, not showing a single island terminating in the middle of a stripe.

The island growth (or Volmer-Weber) is characterized by the nucleation and formation of a second and third layer before the completion of the first ones, as observed in the panel above. For cobalt evaporation times of up to 360 seconds, the characteristic Au(100) reconstruction is still visible beneath the cobalt islands, while 10 minutes of evaporation in the previously defined parameters seems to be enough to cover the whole surface (Fig. 5.2(F)).

While investigating the growth of Co on Au, an additional phenomenon was examined: the diffusion of cobalt into the gold substrate upon heating. In good agreement with the literature [30, 31, 34, 42], several characteristic surface features were observed. These included vacancies with depths of 0.6 Å, attributed to the exchange of an Au atom with a Co atom, and 1.0 Å, corresponding to a height difference between 5 ML Au and 5 ML bcc-Co covered by 1 ML Au. Circular

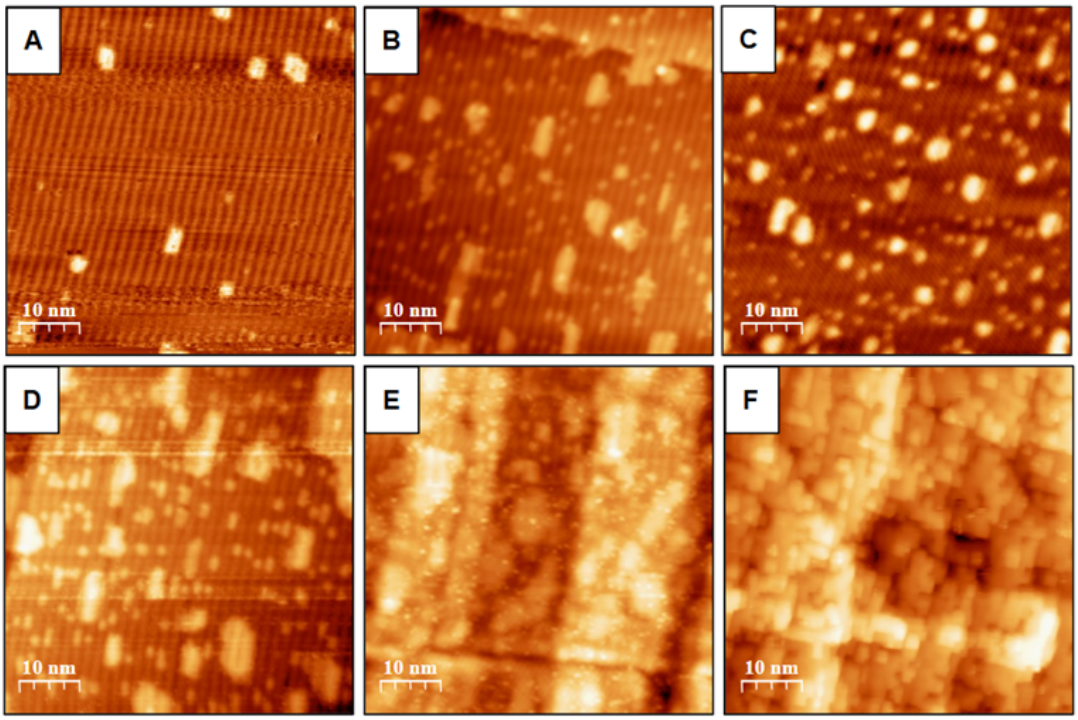

Figure 5.2: *STM images showing the evolution of cobalt islands for different experiments with increasing duration of evaporation. Scanning parameters: (A) 30s: Bias=-800mV and I=500pA, (B) 90s: Bias=1400mV and I=600pA, (C) 120s: Bias=-1000mV and I=600pA, (D) 240s: Bias=1200mV and I=500pA, (E) 360s: Bias=2000mV and I=400pA, and (F) 600s: Bias=2000mV and I=600pA.*

structures with heights of 2.0 Å, assigned to Au adatoms expelled from the surface reconstruction, or integer multiples thereof, as well as structures with heights of 2.8 Å, corresponding to 2 ML of bcc-Co, were also identified. In addition, large reconstructed islands with heights of 3.4 Å, associated with 1 ML bcc-Co covered by 1 ML fcc-Au, showing protrusions with a periodicity of 14 Å, and unreconstructed islands with heights of either 2.78 Å (2 ML bcc-Co) or 2.0 Å (Au islands) were observed. The two domains of the Au(100) reconstruction are rotated by 95° with respect to one another. Furthermore, the reconstruction with stripes oriented along the <01-1> direction exhibits a slightly smaller periodicity of 13.8 Å compared to the 14.5 Å periodicity measured along the <011> direction.

The reappearance of the Au(100) reconstruction after annealing in UHV an Au(100) substrate previously coated with Co for 10 minutes suggests the possible formation of an Au surfactant overlayer covering cobalt-rich regions, as previously reported in the literature [30, 31, 34, 42]. An additional feature observed in this work, which has not been previously reported, is the presence of rectangular islands exhibiting an apparent height of approximately 0.3 Å relative to the surrounding Au(100) reconstruction. The rims of these islands, however, are 0.55-0.75 Å higher than their centers. This morphology can be attributed to a

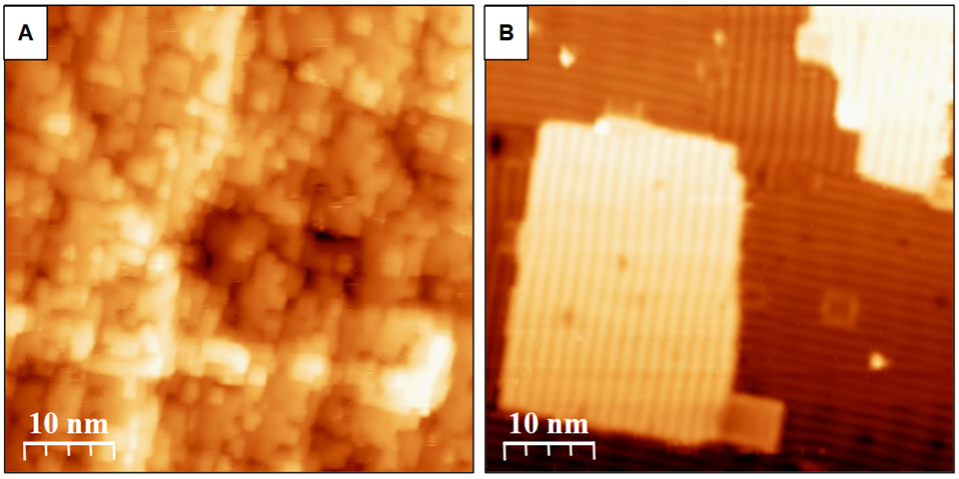

Figure 5.3: *STM image of (A) 10 minutes of cobalt evaporated on Au(100) (Bias=2000mV, I=600pA), and (B) the film from (A) after annealing in UHV for 5 minutes at $T < 373K$ (Bias=2000mV, I=900pA).*

structure with a central region composed of Au atoms and rims consisting of 1 ML of bcc-Co covered by an fcc-Au surfactant overlayer.

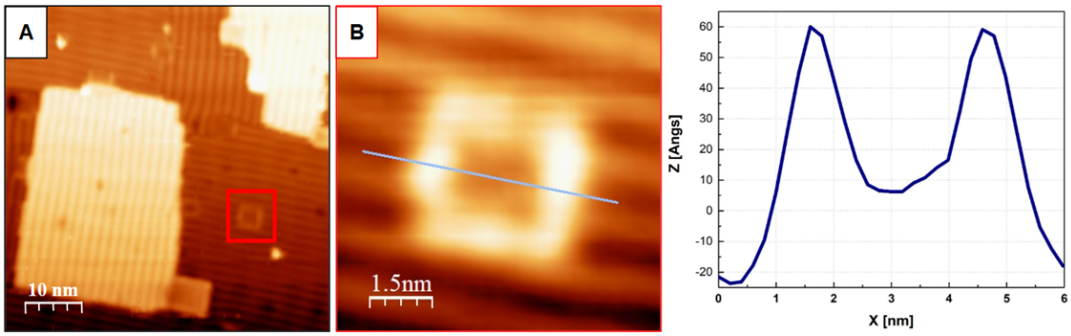

Figure 5.4: *Zoom of Figure 5.3(A) and profile of this structure.*

5.2 Sulfurization of Au(100)

In order to enable the visual distinction between the interactions of sulfur with gold and with cobalt, a series of experiments were performed by exposing the substrate to hydrogen sulfide as a function of the sample's temperature during sulfurization. Those experiments were performed by exposing the sample to a pressure of H_2S of $2.0 \cdot 10^{-5}$mbar for 15 or 30 minutes and heating it at a fixed temperature.

From theoretical studies, the adsorption of H_2S is highly unlikely due to its low-temperature (170K for the (100) facet of gold and 190K for the (111) surface of Au) dissociation from H_2S to $HS* + H$ [80], being a prompted reaction when gaseous hydrogen sulfide interacts with metallic surfaces. With that in mind, the

first experiment was conducted by maintaining the Au(100) substrate at room temperature (RT) while exposing it to a H_2S atmosphere (Fig. 5.5(a)) and the result showed a surface with a great amount of adsorbed material without organization and regions where a linear organization can be seen in the <011> and <01-1> directions of the substrate. Those lines have an apparent distance of 5.56 Å between them, which could be attributed to a poorly imaged zigzag structure as reported by [48]. When maintaining the sample at ~323K during hydrogen sulfide exposure (Fig. 5.5(b)), the final product showed similar features to the previous experiment, lines distancing by 5.6 Å and a great amount of adsorbates without apparent organization, but also a new structure: circular forms with a square-like symmetry distancing by 17.1 Å from each other. This feature might be a sulfur superstructure, as it appears again in a higher temperature exposure.

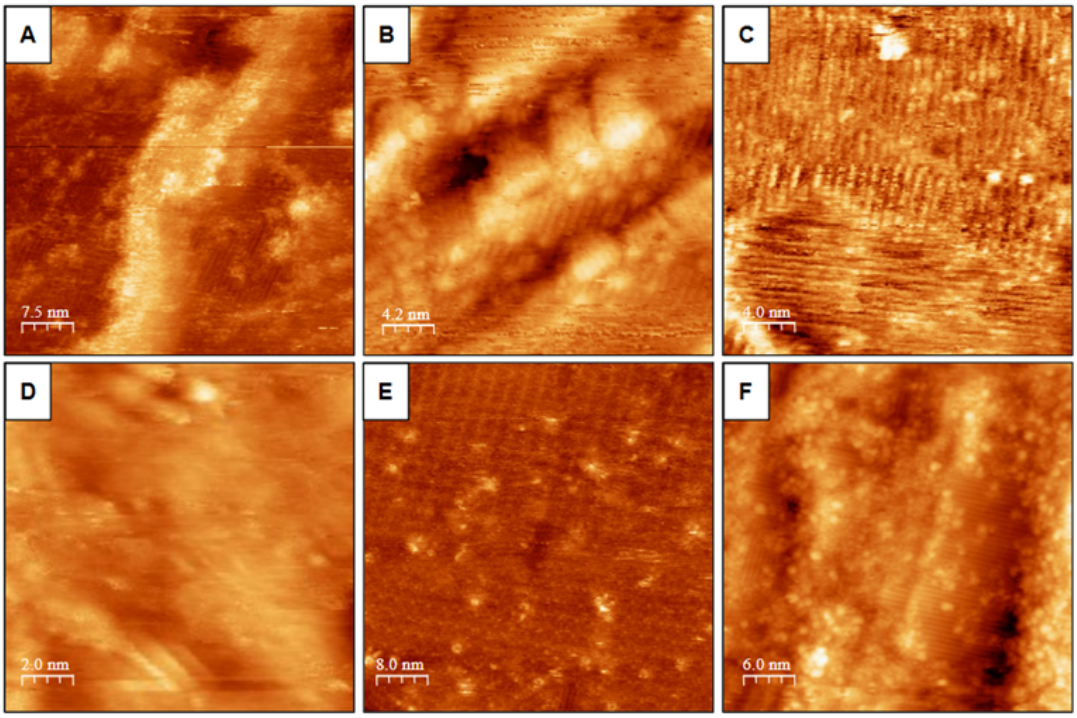

Figure 5.5: *Panel showing STM images corresponding to a clean Au(100) sample sulfurized at a fixed temperature of: (A) Room Temperature (Bias=1200mV and I=800pA), (B) 323K (Bias=960mV and I=756pA), (C) 403K (Bias=1800mV and I=700pA), (D) 543K (Bias=1800mV and I=600pA), (E)643K (Bias=1300mV and I=700pA) and (F) 693K (Bias=-1300mV and I=800pA).*

As the temperature of the sample during sulfurization is increased up to 543 K, adsorbates with higher dynamics are seen on the surface as streaky noise, which diminishes the resolution of the scanned images. When a temperature of ~645 K is reached, the surface turns to a highly organized pattern with small adsorbates on top of it. Two types of structures are seen in Figure 5.5(e): the same circular features with distancing of 17 Å as in the image above it (Fig. 5.5(b)) and a small

region with the already seen lines with a distance of 5.57 Å between them. Raising the temperature up to 693 K during sulfurization (Fig. 5.5(f)) seems to generate a sample that has surpassed the point of saturation and began to agglomerate the excess material on top of it.

The observations described above led to the conclusion that an ideal temperature for the adsorption of atomic sulfur and other sulfur coordinated complexes for the Au(100) surface was determined to be slightly below 643 K, for which a post-annealing in UHV would be unnecessary.

Some distinguished features attributed to the Au-S interaction were also present on cobalt sulfide growth experiments. Figure 5.6(a) shows a square-like structure with side length of 8 Å, which was reported in the literature as composed of 8 S atoms around a gold atom with a side length of 5 Å. The difference in the side length of the structures could indicate a larger sulfur complex composed of double the amount of sulfur atoms ([52] defines the S-S distance as 2.05Å). In Figure 5.6(b) what was called a sulfur superstructure is imaged above the previously described linear pattern with the characteristic 5.61 Å distance between them. And, lastly, the third image on Fig. 5.6 displays the p(2×2) sulfur pattern already reported in the literature ([47–49, 52]) with what might be Au-S complexes on top.

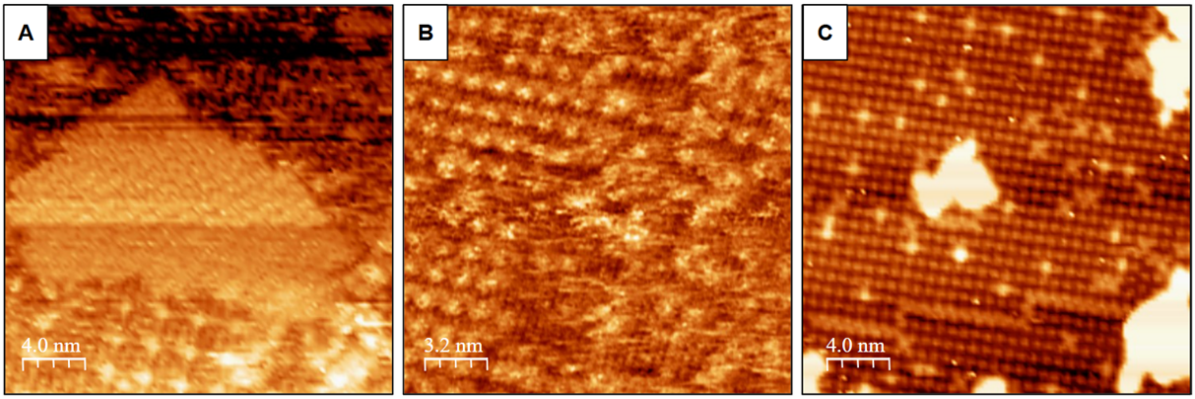

Figure 5.6: *STM images showing structures related to the interaction of Sulphur and Gold: (A) square-like feature with sides with* 8.04 ± 0.03 *Å length (Bias=1200mV and I=500pA), (B) stripes with distancing of 5.77 Å below what seems to be a sulphur superstructure with square pattern and distance of* 17.1 ± 0.3 *Å (Bias=1100mV and I=700pA), and (C) possible* Au_xS *complexes (Bias=900mV and I=700pA).*

Although *Walen et al.* [49] imaged these Au_xS complexes with a low temperature STM, which is expected to diminish the mobility of sulfur atoms, Figure 5.6(C) is imaged at room temperature and in a completely different scenario. While Au_xS complexes studied by *Walen et al.*[49] were formed by deposition of sulfur in situ via an electrochemical Ag|AgI|Ag_2S|Pt source, Fig. 5.6(C) was ob-

tained after sulfurizing cobalt oxide islands at a temperature slightly above RT (∼323 K). The similar features imaged after distinct experiments could indicate that sulfur atoms might have their dynamic properties decreased by the creation of local strain fields caused by the coexistence and/or association of cobalt oxide and sulfide structures. Since adatom diffusion barriers are extremely sensitive to the local atomic geometry, even small strain fields can have a great impact in the surface mobility of this atoms.

5.3 Growth of CoO_x/Au(100)

A second path for the growth of cobalt sulfide was to sulfurize a cobalt oxide film grown on Au(100). In order to understand the transition from oxide to sulfide, experiments of cobalt oxide growth with coverages lower than the amount required to cover the entire Au surface were performed. Sulfurization of metal oxides was applied as a pathway to grow cobalt sulfide films because of the lower temperatures required for the formation of metallic oxides and the high tendency of oxygen to react with H_2S to generate water molecules [81].

The first grown cobalt oxide structures were irregular hexagonal islands with a square symmetry of its atoms and an interatomic spacing of 3.1 ± 0.1 Å, which corresponds to the (100) facet of CoO. Before annealing the sample in the same oxygen atmosphere as the evaporation, the Au surface showed a great amount of steps with the CoO(100) hexagonal islands growing from its edges. After annealing in oxygen pressure, the Au surface beneath the cobalt oxide islands was flat, the CoO islands coalesced but maintained its atomic pattern with a slight distortion in its interatomic spacing and the appearance of in-line vacancies, vacancies in fourfold hollow sites and bright structures on-top sites on the CoO surface. As the image was acquired with atomic resolution, the apparent heights and depths of these features may be affected by the local electronic structure and therefore may not accurately represent their actual topographic dimensions. After annealing the sample in a O_2 atmosphere, the island size grew from approximately 115 nm^2 to 2070 nm^2, likely due to the temperature-enhanced mobility of Co on Au surfaces.

The reason why the islands have a hexagonal shape but show a square atomic pattern is not fully understood yet. A possibility is that the Au(100) reconstruction is lifted locally, which causes the cobalt oxide islands to have a square-like atomic pattern (unreconstructed Au below it) while a hexagonal limitation of its area (hexagonal symmetry Au surface in the surroundings). Another feature observed was that islands with different heights showed slightly different orientations of its atomic patterns, while maintaining the square symmetry. Though Figure

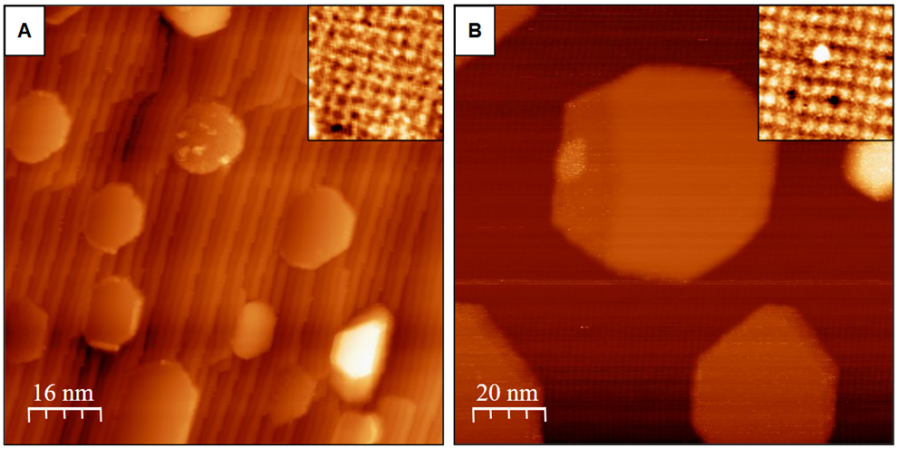

Figure 5.7: *STM images showing the influence of post-annealing cobalt oxide structure in a $p(O_2)$ atmosphere: (A) As-grown cobalt oxide islands, Bias=1800mV and I=500pA. Inset size: 3.0 nm x 3.0 nm, and (B) post-annealed cobalt oxide islands, Bias=1000mV and I=700pa. Inset: Bias= -500mV and I=1200pA (3.0 nm x 3.0 nm).*

5.7 shows two different islands of CoO(100), both of them display a square atomic pattern oriented in the <011> direction of Au(100), which might indicate that they have an equal amount of monolayers of cobalt oxide. On the other hand, Figure 5.8(B) clearly demonstrates a rotation of 35° on the atomic pattern of the CoO island. This is likely due to a ∼5% mismatch between the CoO(100) surface lattice constant (3.03 Å) and the Au(100) surface lattice constant (2.88 Å), which becomes more pronounced with a larger number of CoO monolayer stacked over each other.

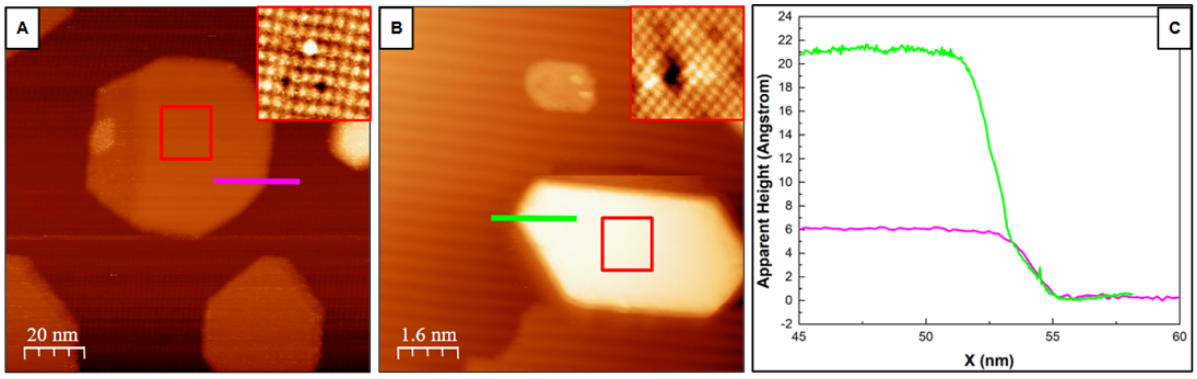

Figure 5.8: *STM images showing: (A) a 6.16 Å high (∼3ML) CoO island with inset showing the square atomic pattern in the directions with greater symmetry of Au(100), (B) a 1.5nm high (∼7ML) CoO island with inset showing the square atomic pattern rotated by approximately 35° clockwise compared to the inset on (A), and (C) Height profile of the pink line in (A) and green line in (B). Scanning parameters were: (A) Bias=1000mV and I=700pA for the survey, Bias=-500mV, and I=1200pA for the inset (3.0nm x 3.0nm); (B) Bias=800mV and I=900pA for the survey and inset (3.0nm x 3.0nm).*

XPS measurements were performed to analyze the chemical composition of the cobalt oxide film, which cannot be accessed by the STM. Figure 5.9 shows

the survey of a cobalt oxide grown and post-annealed over the substrate, the high resolution spectrum of Co 2p with black arrows highlighting the characteristic satellites peaks of CoO and the high resolution spectrum of O 1s. The quantification obtained by the survey spectrum shows an approximately Co:O ratio of 1:1, confirming the stoichiometry suggested by the atomic resolution of STM images. In Fig. 5.9(b), a characteristic satellite peak can be seen for each component of the Co 2p high resolution spectrum with an energy separation of ~6.5eV from the satellites to the main peak [82, 83]. The two main peaks, corresponding to *Co* $2p3_{3/2}$ and *Co* $2p_{1/2}$, have a separation of ~15.9eV [82, 83].

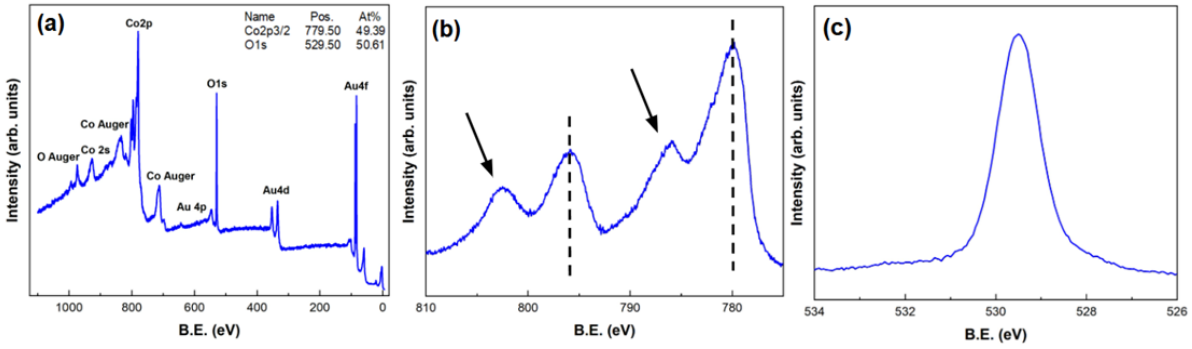

Figure 5.9: *XPS spectra of Cobalt Oxide grown over Au(100): (a) survey, (b) Co 2p and (c) O 1s.*

As a larger quantity of cobalt oxide is grown over the (100) surface of gold, other features that seem to be caused by a rotated CoO(100) pattern over the previously grown CoO(100) in the <011> direction of Au(100) appear. Figure 5.10 shows a survey STM image with 4 different areas: the reconstructed surface (100) of Au, a lower region with a 87 Å periodicity Moiré pattern (labeled 1), a higher region with a different moiré pattern with a in-line periodicity of 27.1 Å (labeled 2) and a unreconstructed area with a height of 4.42 Å compared with the reconstructed Au(100). The lower region (1) has a apparent depth of 6.39 Å with its left rim being 6.54 Å higher than the reconstructed area and the right rim having a height of 8.51 Å compared to the reconstructed area on the right side of this region. This Moiré pattern doesn't show an hexagonal symmetry, but rather a poorly resolved square-like symmetry with its lower regions being aligned both on horizontal and vertical directions. The unreconstructed region (3) has a apparent height of 4.42 Å compared to the reconstructed area and 6.48 Å when compared to region 1. Region 2 shows a linear Moiré pattern with adjacent lines being 27 Å apart and intercalating higher and lower lines with a maximum height variation of 1.56 Å. This linear Moiré pattern, as seen in the reconstruction of Au(100), can be produced by the existence of two layers of material with different

symmetries: an upper layer with a hexagonal symmetry and a lower layer with a square symmetry. Because region (1) has a lower height than the reconstructed area, it is reasonable to assume that the gold atoms were expelled from this place, likely mixing with the cobalt sulfide phase on the unreconstructed areas as region (3), on the rims of region (1) or even coalescing on the reconstructed surface forming Au steps, as can be seen in the lower right side of the survey on Figure 5.10.

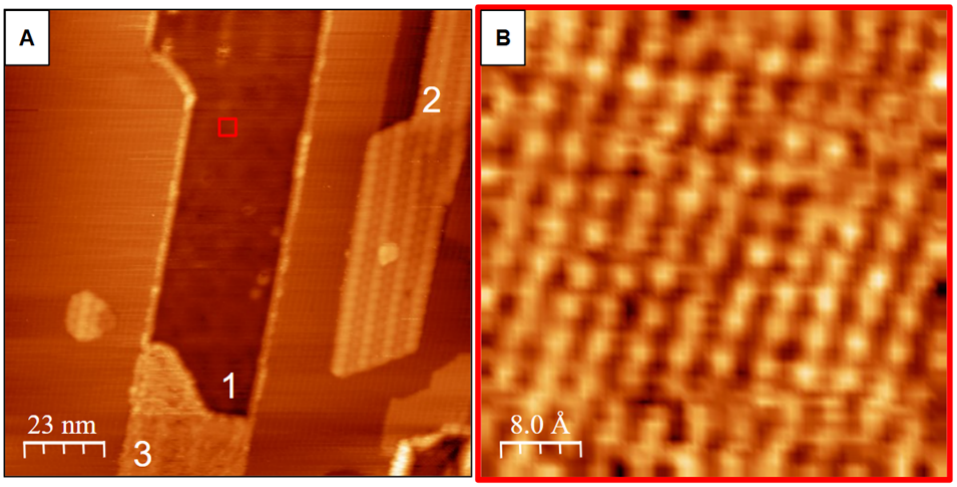

Figure 5.10: *STM survey image (A) showing structures with different patterns found when growing cobalt oxide (Bias=1100mV and I=400pA) and a zoom in (B) showing the atomic square pattern with 3.01Å and 2.84Å sides inside the red square marked on (A).*

Cobalt oxide structures with Moiré patterns were reported in the literature, but mainly on cobalt oxide films grown on (111) facets [60, 61, 64], which resulted in atomic hexagonal patterns and hexagonal Moiré patterns.

As previously reported in the results about the growth of metallic cobalt over Au(100), when exposed to temperature cobalt has a high tendency to diffuse into the substrate. In order to grow a cobalt sulfide film, this path was considered because initiating sulfurization with a cobalt oxide film was less likely to result in interdiffusion between cobalt and gold. The following section describes the cobalt sulfide film obtained by sulfurizing the CoO film.

5.4 CoS_x film on Au(100)

In order to obtain a crystalline cobalt sulfide film, two different approaches were explored: the sulfurization of metallic cobalt evaporated onto Au(100) at room temperature and the sulfurization of a crystalline cobalt oxide film previously grown on Au(100). For the first approach, a series of experiments was performed at temperatures ranging from room temperature to 623 K, with the temperature

kept constant during each individual experiment, while keeping the remaining experimental parameters constant: H_2S pressure of $2.0 \cdot 10^{-5}$ mbar and exposure time of 30 min. For the second approach, the previously grown cobalt oxide film was sulfurized for a longer period while maintaining the same H_2S pressure and a constant sample temperature.

The first approach presented several challenges arising from the factors discussed previously in this chapter: (1) the instability of cobalt on Au(100) upon exposure to even relatively low temperatures and (2) the formation of different Au(100) surface reconstructions upon exposure to an H_2S atmosphere. These characteristics resulted in stringent experimental requirements and rendered the resulting surface highly sensitive to even minor variations in the experimental conditions. Therefore, a second approach was investigated, consisting of the sulfurization of a previously grown crystalline cobalt oxide film. As reported in the literature, this approach requires lower temperatures than the sulfurization of metallic cobalt and favors the formation of crystalline cobalt sulfide. The oxygen present in the cobalt oxide film has a strong tendency to react with the hydrogen from the H_2S atmosphere, facilitating the sulfurization process at lower temperatures. Combined with the greater likelihood of obtaining a crystalline cobalt sulfide film through the sulfurization of a pre-existing crystalline cobalt oxide film, these characteristics make this approach a promising alternative for the preparation of cobalt sulfide films.

An unexpected result was obtained when the second approach for the growth of cobalt sulfide was employed. After sulfurization of a thicker CoO film than that described above, the resulting cobalt sulfide film exhibited a hexagonal atomic pattern rather than the square-like pattern expected from the symmetry of the underlying substrate. This change in surface symmetry may occur at two different stages of the preparation. First, if the CoO film is sufficiently thick, the film may initially adopt a (100) orientation at the interface with the substrate and subsequently develop a (111) orientation at the surface, driven by the energetic favorability of this arrangement. This transition could result in modifications to the final symmetry observed in the film. Alternatively, the change in surface orientation may occur during the sulfurization process as the CoO is converted into Co_3S_4. The latter adopts a spinel structure, for which the (111) surface is generally energetically favorable due to its high atomic density and reduced number of dangling bonds. The second hypothesis is further supported by the fact that cobalt sulfide films commonly require post-sulfurization annealing under UHV conditions. This step is necessary to eliminate the water produced during the sulfurization process, as described by Reaction 5.1. The additional thermal

energy supplied during annealing may provide sufficient mobility for the atoms in the film to rearrange into a more energetically favorable configuration. As discussed above, such a configuration may correspond to a $Co_3S_4(111)$ surface.

$$4H_2S_{(g)} + 3CoO_{(s)} \rightarrow Co_3S_4(s) + 3H_2O(g) + H_{2(g)} \tag{5.1}$$

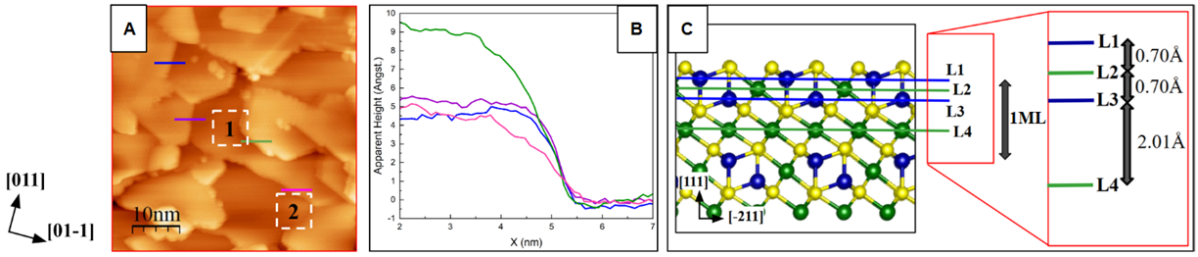

Figure 5.11: *(A) STM image showing the structure of the $Co_3S_4(111)$ film grown with scanning parameters: Bias=-200mV and I=700pA, (B) Height profile of structures seem on (A), and (C) Side view of $Co_3S_4(100)$ structure generated with VESTA. Black arrows on the left side of (A) indicate the high symmetry substrate directions.*

Analysis of the STM images yielded an interatomic distance of 6.8 ± 0.6 Å. Comparison with crystal structures analyzed using VESTA suggests that the observed structure may correspond to the (111) facet of one of three cobalt sulfide phases: CoS_2, for which the S–S distance is 7.8 Å; Co_3S_4, for which the Co–Co distance is 6.6 Å; or Co_9S_8, for which the Co–Co distance is 6.9 Å. Analysis of Figure 5.11 and the corresponding step-height profiles allowed exclusion of the CoS_2 with S termination, as the experimental step heights were significantly larger than the 3.18 Å expected for this bulk structure. The height profiles of several steps, indicated by the colored lines in Figure 5.11(A), are presented in Figure 5.11(B). The measured step heights were approximately 5.43 Å or integral multiples thereof. This value was assigned to 1 ML of Co_3S_4, as illustrated in Figure 5.11(C). In this model, L1 and L3 correspond to layers of Co^{2+} atoms, whereas L2 and L4 correspond to layers of Co^{3+} atoms. Both L1 and L2 exhibit the same hexagonal atomic symmetry, as shown in Figure 5.12(C) and (D). Based on a qualitative analysis of undercoordinated sulfur atoms and the surface polarity arising from cobaltsulfur separation, a Co^{2+}-terminated surface is expected to be the most favorable configuration after surface relaxation.

To further investigate this question, XPS measurements were performed (Fig. 5.14). The Co_9S_8 phase was ruled out on the basis of the Co-to-S ratio obtained from elemental quantification. Consequently, the surface observed by Scanning Tunneling Microscopy was attributed to $Co_3S_4(111)$. The cobalt sulfide film exhibited two domains with different orientations of the hexagonal pattern. In the

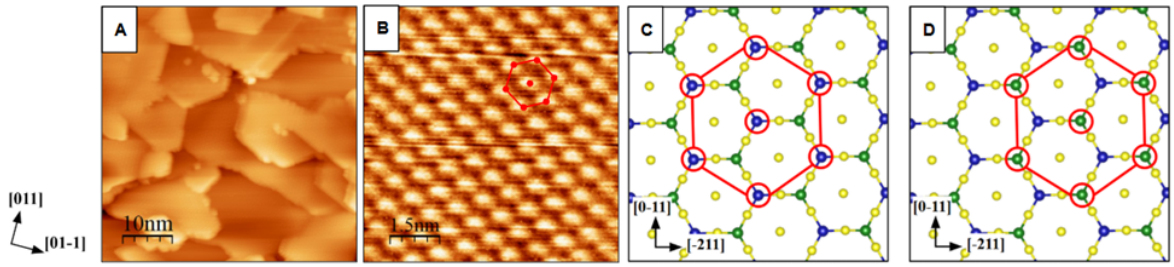

Figure 5.12: *(A) $Co_3S_4(111)$ film, (B) Hexagonal atomic pattern of the film in (A), (C) Top view of a $Co_3S_4(111)$ surface with Co^{+2} termination, and (D)Top view of a $Co_3S_4(111)$ surface with Co^{+3} termination. Atoms in blue are cobalt with valency +2, atoms in green are cobalt with valency +3, and atoms in yellow are sulfur. Scanning Parameters: (A) Bias = -200mV and I = 700pA, (B) Bias = -250mV and I = 800pA. Black arrows on the left side of (A) indicate the high symmetry substrate directions.*

domain highlighted in blue (Fig. 5.13(A)), the high-symmetry directions of the hexagonal structure are parallel to the [011] direction of the substrate, whereas in the domain highlighted in red (Fig. 5.13(B)), the high-symmetry directions are parallel to the [01-1] direction of the substrate.

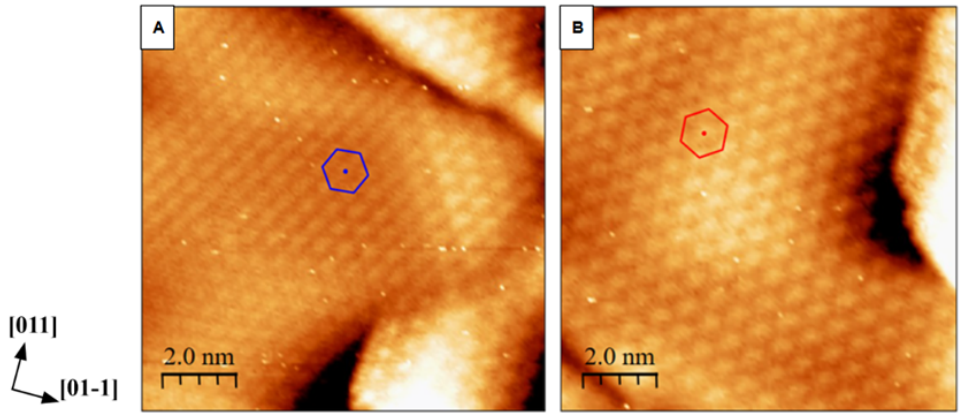

Figure 5.13: *STM images showing two different domains in the hexagonal atomic pattern of the film. (A) High symmetry directions of the blue hexagon parallel to the [01-1] direction of the substrate, and (B) High symmetry directions of the red hexagon parallel to the [011] direction of the substrate. Zoom in of Figure 5.11(A). Black arrows on the left side of (A) indicate the high symmetry substrate directions.*

As mentioned in the previous section, the energy separation between the $Co\ 2p_{3/2}$ and $Co\ 2p_{1/2}$ peaks is approximately 14.9 eV, as shown in Figure 5.14(b). Comparison of the high-resolution Co 2p spectra obtained by XPS for the cobalt oxide film (Fig. 5.14(b)) and the cobalt sulfide film (Fig. 5.14(b)) indicates that the cobalt oxide was almost completely sulfurized. In addition, the STM images presented in Figures 5.11, 5.12, and 5.13 are consistent with the formation of a $Co_3S_4(111)$ surface. Elemental quantification based on the areas of the $Co\ 2p_{3/2}$ and $S\ 2p$ peaks in the survey spectrum of the cobalt sulfide sample yielded a Co:S ratio of approximately 43:57, which is consistent with the 3:4 stoichiometric ratio

expected for Co_3S_4. The high-resolution $S\ 2p$ spectrum shown in Figure 5.14(c) indicates the presence of sulfur atoms in different chemical environments. This observation is consistent with the presence of cobalt in distinct coordination environments (Fig. 5.14(b)), including Co^{2+} and Co^{3+} sites, providing further support for interpreting the film as Co_3S_4-like.

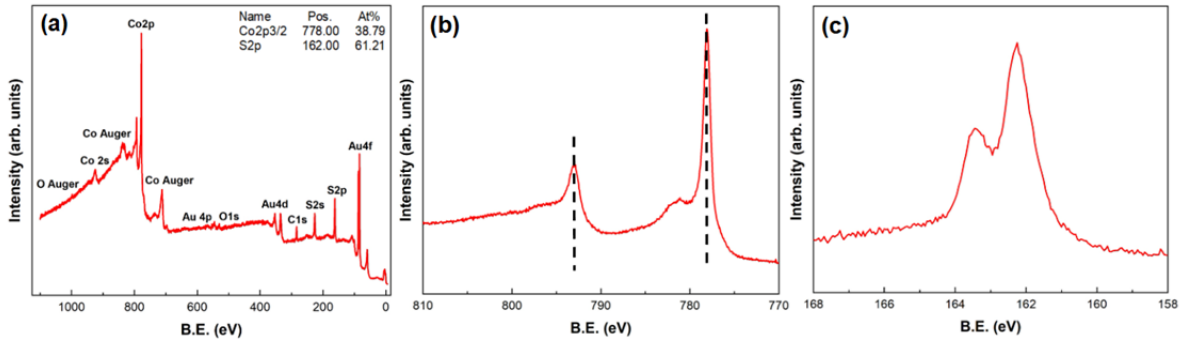

Figure 5.14: *Panel showing XPS spectra of the sulfurized cobalt oxide sample: (a) survey, (b) Co 2p and (c) S 2p.*

The high-resolution $Co\ 2p_{3/2}$ and $S\ 2p$ spectra reported in the literature were obtained from cobalt sulfide nanostructures grown on different substrates. These spectra exhibit considerable similarity among the different cobalt sulfide phases, making definitive phase identification challenging, particularly when analyzing a continuous film such as that investigated in the present work.

Conclusion and Future Perspectives

The results presented in this work demonstrate the importance of each stage of the experimental investigation in enabling the unambiguous identification of the cobalt sulfide structures observed by STM. The nucleation of cobalt nanoparticles was found to occur preferentially in regions of higher local density of states on the Au(100) surface, while subsequent Co deposition followed a growth mechanism consistent with mechanisms previously reported for other transition metals. Exposure of the clean Au(100) surface to an H_2S atmosphere produced sulfur structures consistent with the literature, although previously unreported sulfur structures were identified in the present work. Furthermore, no studies describing cobalt oxide or cobalt sulfide growth on Au(100) had been reported in the literature prior to this work. Consequently, this thesis provides the first description of the growth of CoO(100) islands and a continuous $Co_3S_4(111)$ film on the Au(100) surface, through STM and XPS.

This Thesis also establishes a methodological framework for the preparation of relatively thick cobalt sulfide films through the sulfurization of cobalt oxide films by exposure to hydrogen sulfide at intermediate and elevated temperatures. In contrast to previous studies, the methodology presented here enables the preparation of well-defined, continuous cobalt sulfide films, potentially suitable for thermal and electrocatalytic investigations. As a result, this work opens new opportunities for the preparation and investigation of two-dimensional cobalt sulfide films.

Future studies should focus on determining the surface termination of the Co_3S_4 film by probing the surface with CO molecules and performing FTIR-IRRAS measurements to identify the metallic sites exposed at the surface. In addition, collaboration with a theoretical research group to investigate the stability of possible surface terminations could provide valuable insights into the atomic structure of the film. Finally, STM investigations under ultra-high vacuum conditions could be employed to study the adsorption and dissociation of water molecules on the Co_3S_4 surface, contributing to a deeper understanding of its potential catalytic activity.

Appendix A:

NANONIS Mimea Software

The electronic used in this research was the SPECS NANONIS Mimea Electronics. Through its interface, it is possible to control the scanning parameters (3 - tunneling current, bias, proportional and integral error correction or time constant error correction, 9 - scan velocity), image parameters (9 - size, direction and angle of scanning, file name, tilt correction), piezoelectric configuration (7 - upper, lower and central voltage when moving and relaxing) and real-time noise information (2 - through the FFT analyzer). An additional feature of this software is tracking the tunneling current measured by the tip and the tip-surface distance in real time (windows marked 1, 5 and 6).

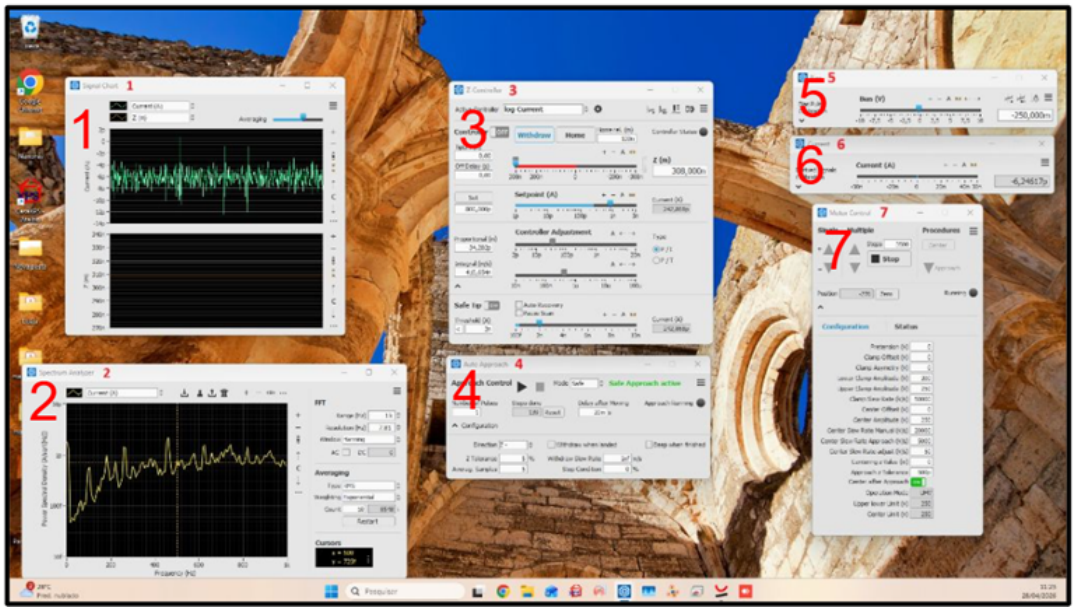

Figure 5.15: *NANONIS Mimea interface tabs 1-7. Print screen of the computer.*

When starting the NANONIS Mimea interface, the user can personalize the windows the software will keep open and its visual organization on the computer screen. The first crucial step when measuring a sample with the STM microscope is to set the bias applied to the sample (5), the tunneling current setpoint (3), and

the Proportional and Integral parameters (3) without causing a crash between the tip and the sample's surface. These values are extremely important when activating the "Safe-Approach" (4) because the bias applied is strongly related to the tunneling current that the system will measure, which has a high dependence on the tip-sample distance, and the P-I parameters will control how quickly the steps will be taken. Using the "Safe Approach", the Approach control (4) unit works by walking a step closer to the sample and measuring the tunneling current, if the current is lower than the one set by the user, the tip takes another step forward and so on. Using this tool, the tip approach can be done in a safer way, ensuring more precise movement than by choosing the number of steps without being aware of how close the tip is to the sample. The parameters on windows 7 can be changed by the user if an unbalanced movement between the piezoelectric sections is noticed, controlling the tensions present in the inchworm movement, explained in Section 4.4.2.

As mentioned in the previous subsection, the feedback system ensures a better output from the experiment. The feedback system for the Nanonis Mimea electronics is a PI-feedback (Proportional-Integral Feedback) that works by applying a proportional and integral (or time constant) gain, both values selected by the user when acquiring an image. The proportional gain is related to the current error of the measure, while the integral gain is related to the sum of past errors that may have persisted over time. If the proportional gain is too high, it can cause oscillations that may be correlated with the frequency of the scanner, while a low value can result in the loss of information due to the slow reaction of the feedback. For the integral gain, a high value can cause again oscillations in the current, while a low value implies a struggle to compensate steps on the sample's surface.

Windows 8 and 9 show the current image and z-distance image in real time, respectively. It is possible to change the color scale, the image contrast and visualized region for each windows. Section 9 also controls the scanning line speed and the speed perpendicular to the scanning direction, the scanning direction, the image size, the scanned area of the sample, tilt parameters, number of pixels per image, and the image's name when saved. A countdown can be found on the upper right region of tab 9 indicating the time left to finish obtaining the current image. The tip tilt is applied to minimize the z-distance variation due to a sample inclination that might be caused by sample mounting, UHV cleaning or fitting the sample holder in the microscope. It is crucial to change the direction of scanning when varying the tilt in the same direction, using tab 1 to control the z distance. Lastly, tab 9 allows the NANONIS Mimea user to stamp the measured images,

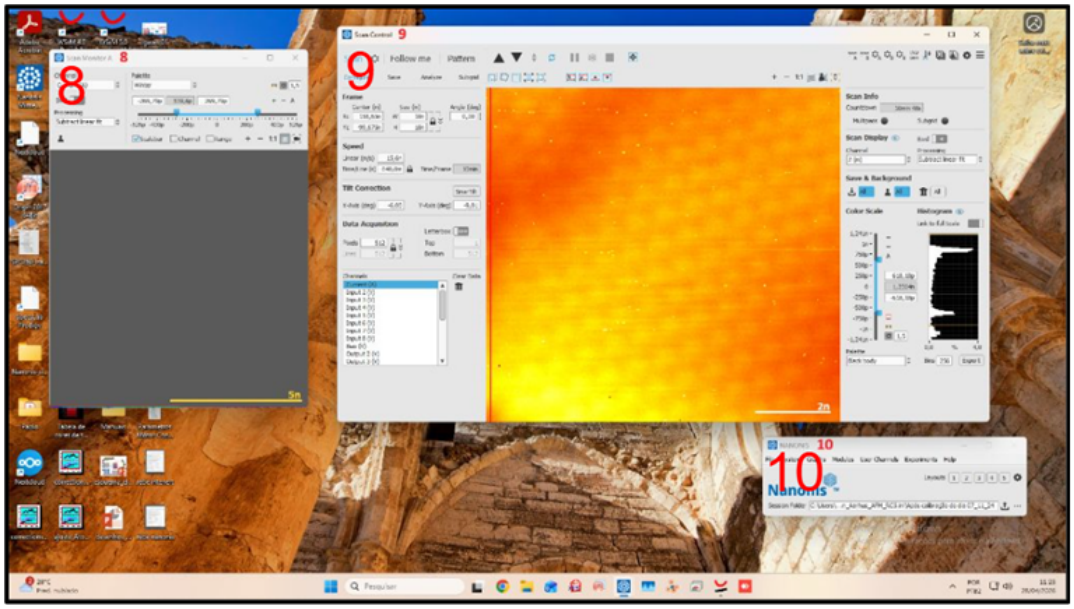

Figure 5.16: *NANONIS Mimea interface tabs 8-10. Print screen of the computer.*

which indicates where the previous images were scanned, and automatically save each scanned image.

Tab 10 controls the creation of a new session (same pathway where the images will be saved), the piezoelectric configuration (constant value of mV/nm set by the user when calibrating the microscope) and where the software can be exited.

This software also features a demo mode for training the user with an ideal virtual sample before measuring a real material.

Bibliography

[1] C.-H. Lai, M.-Y. Lu, L.-J. Chen, Metal sulfide nanostructures: synthesis, properties and applications in energy conversion and storage, J. Mater. Chem. 22 (2012) 19–30. doi:10.1039/C1JM13879K.
URL http://dx.doi.org/10.1039/C1JM13879K 1, 3.4

[2] P. J. Masset, R. A. Guidotti, Thermal activated (thermal) battery technology: Part iiib. sulfur and oxide-based cathode materials, Journal of Power Sources 178 (1) (2008) 456–466. doi:https://doi.org/10.1016/j.jpowsour.2007.11.073.
URL https://www.sciencedirect.com/science/article/pii/S0378775307026146 1, 1.2, 3.4

[3] J.-S. Chung, H.-J. Sohn, Electrochemical behaviors of cus as a cathode material for lithium secondary batteries, Journal of Power Sources 108 (1) (2002) 226–231. doi:https://doi.org/10.1016/S0378-7753(02)00024-1.
URL https://www.sciencedirect.com/science/article/pii/S0378775302000241 1, 3.4

[4] H. K. Mulmudi, S. K. Batabyal, M. Rao, R. R. Prabhakar, N. Mathews, Y. M. Lam, S. G. Mhaisalkar, Solution processed transition metal sulfides: application as counter electrodes in dye sensitized solar cells (dscs), Phys. Chem. Chem. Phys. 13 (2011) 19307–19309. doi:10.1039/C1CP22817J.
URL http://dx.doi.org/10.1039/C1CP22817J 1, 3.4

[5] L. Zhang, H. B. Wu, X. W. D. Lou, Unusual cos2 ellipsoids with anisotropic tube-like cavities and their application in supercapacitors, Chem. Commun. 48 (2012) 6912–6914. doi:10.1039/C2CC32750C.
URL http://dx.doi.org/10.1039/C2CC32750C 1

[6] S. Aloqayli, C. Ranaweera, Z. Wang, K. Siam, P. Kahol, P. Tripathi, O. Srivastava, B. K. Gupta, S. Mishra, F. Perez, X. Shen, R. K. Gupta, Nanostructured cobalt oxide and cobalt sulfide for flexible, high performance

and durable supercapacitors, Energy Storage Materials 8 (2017) 68–76. doi:https://doi.org/10.1016/j.ensm.2017.05.006.
URL https://www.sciencedirect.com/science/article/pii/S2405829717300703 1, 3.4

[7] J. Bonde, P. G. Moses, T. F. Jaramillo, J. K. Nørskov, I. Chorkendorff, Hydrogen evolution on nano-particulate transition metal sulfides, Faraday Discuss. 140 (2009) 219–231. doi:10.1039/B803857K.
URL http://dx.doi.org/10.1039/B803857K 1, 3.4

[8] W. Zhu, X. Yue, W. Zhang, S. Yu, Y. Zhang, J. Wang, J. Wang, Nickel sulfide microsphere film on ni foam as an efficient bifunctional electrocatalyst for overall water splitting, Chem. Commun. 52 (2016) 1486–1489. doi:10.1039/C5CC08064A.
URL http://dx.doi.org/10.1039/C5CC08064A 1, 3.4

[9] Z. Zhang, Y. Wang, S. Ying, C. Yang, J. Zhao, N. Hu, C. Peng, In-situ sulfidation-derived three-dimensional cobalt sulfide nanoflower/graphene nanosheet hybrid for ultrasensitive room-temperature no2 gas sensor, Journal of Alloys and Compounds 926 (2022) 166868. doi:https://doi.org/10.1016/j.jallcom.2022.166868.
URL https://www.sciencedirect.com/science/article/pii/S0925838822032595 1

[10] H. Zhou, K. Xu, N. Ha, Y. Cheng, R. Ou, Q. Ma, Y. Hu, V. Trinh, G. Ren, Z. Li, J. Z. Ou, Reversible room temperature h2 gas sensing based on self-assembled cobalt oxysulfide, Sensors 22 (1) (2022). doi:10.3390/s22010303.
URL https://www.mdpi.com/1424-8220/22/1/303 1

[11] G. K. . E. E.-F. H.M. El Sharkawy, Photocatalytic and theoretical study of cos nanoparticles for sustainable dye removal from wastewater, Scientific Reports 15 (1) (2025). doi:10.1038/s41598-025-13932-1.
URL https://doi.org/10.1038/s41598-025-13932-1 1, 3.4

[12] H. Gomaa, Y. Zhai, T. Wang, C. An, A. Lee, Q. Deng, N. Hu, Morphology-performance relationship in hollow-sphere cobalt sulfide photocatalysts for solar-light-driven dye degradation: Integration of rsm, dft, and machine learning, Journal of Environmental Chemical Engineering 13 (6) (2025) 119235. doi:https://doi.org/10.1016/j.jece.2025.119235.
URL https://www.sciencedirect.com/science/article/pii/S2213343725039314 1, 3.4

[13] F. Jamal, A. Rafique, S. Moeen, J. Haider, W. Nabgan, A. Haider, M. Imran, G. Nazir, M. Alhassan, M. Ikram, Q. Khan, G. Ali, M. Khan, W. Ahmad, M. Maqbool, Review of metal sulfide nanostructures and their applications, ACS Applied Nano Materials 6 (9) (2023) 7077–7106. arXiv:https://doi.org/10.1021/acsanm.3c00417, doi:10.1021/acsanm.3c00417.
URL https://doi.org/10.1021/acsanm.3c00417 1

[14] P. H. Edwards, J. R. Bairan Espano, J. E. Macdonald, Rational phase control in the synthesis of cobalt sulfides, Chemistry of Materials 36 (15) (2024) 7186–7196. arXiv:https://doi.org/10.1021/acs.chemmater.4c00911, doi:10.1021/acs.chemmater.4c00911.
URL https://doi.org/10.1021/acs.chemmater.4c00911 1, 3.4

[15] S. Mane, S. Kamble, L. Deshmukh, Cobalt sulphide thin films: Chemical bath deposition, growth and properties, Materials Letters 65 (17) (2011) 2639–2641. doi:https://doi.org/10.1016/j.matlet.2011.05.117.
URL https://www.sciencedirect.com/science/article/pii/S0167577X11006367 1

[16] N. Kumar, N. Raman, A. Sundaresan, Synthesis and properties of cobalt sulfide phases: Cos2 and co9s8, Zeitschrift für anorganische und allgemeine Chemie 640 (6) (2014) 1069–1074. arXiv:https://onlinelibrary.wiley.com/doi/pdf/10.1002/zaac.201300649, doi:https://doi.org/10.1002/zaac.201300649.
URL https://onlinelibrary.wiley.com/doi/abs/10.1002/zaac.201300649 1, 3.4

[17] K. Momma, F. Izumi, *VESTA3* for three-dimensional visualization of crystal, volumetric and morphology data, Journal of Applied Crystallography 44 (6) (2011) 1272–1276. doi:10.1107/S0021889811038970.
URL https://doi.org/10.1107/S0021889811038970 1.3, 4.9

[18] F. Bechstedt, Principles of Surface Physics, Springer Berlin, Heidelberg, 2003. 2.1, 2.4, 2.2, 2.5

[19] S. H. Simon, The Oxford Solid State Basics, Oxford University Press, 2013. 2.2

[20] R. Sewak, C. C. Dey, D. Toprek, Temperature induced phase transformation in co, Scientific Reports 12 (2022) 10054. doi:10.1038/s41598-022-14302-x.
URL https://doi.org/10.1038/s41598-022-14302-x 2.1.1, 3.1

[21] C. Kittel, Introduction to Solid State Physics, Wiley, 1953. 2.3

[22] Z. Cai, B. Liu, X. Zou, H.-M. Cheng, Chemical vapor deposition growth and applications of two-dimensional materials and their heterostructures, Chemical Reviews 118 (13) (2018) 6091–6133, pMID: 29384374. arXiv:https://doi.org/10.1021/acs.chemrev.7b00536, doi:10.1021/acs.chemrev.7b00536.
URL https://doi.org/10.1021/acs.chemrev.7b00536 2.2

[23] J. Friedrich, Methods for bulk growth of inorganic crystals, in: T. Chakraborty (Ed.), Encyclopedia of Condensed Matter Physics, 2nd Edition, Academic Press, Oxford, 2024, pp. 190–207. doi:https://doi.org/10.1016/B978-0-323-90800-9.00087-1.
URL https://www.sciencedirect.com/science/article/pii/B9780323908009000871 2.2

[24] H. Lüth, Solid Surfaces, Interfaces and Thin Films, Springer Cham, 2014. 2.6, 2.7

[25] Z. Ding, P. M. Thibado, C. Awo-Affouda, V. P. LaBella, Electron-beam evaporated cobalt films on molecular beam epitaxy prepared gaas(001), Journal of Vacuum Science Technology B: Microelectronics and Nanometer Structures Processing, Measurement, and Phenomena 22 (4) (2004) 2068–2072. doi:10.1116/1.1771674.
URL https://doi.org/10.1116/1.1771674 2.8

[26] E. Meyer, H. J. Hug, R. Bennewitz, Scanning Probe Microscopy: The Lab on a Tip, Springer, 2004. 2.4.1, 2.4.1, 2.11, 2.4.2, 2.4.2, 2.4.2, 2.4.2

[27] P. M. Bazant, Lecture 20: Quantum tunneling of electrons, Oper Course Lecture (2014). 2.4.1, 2.4.1

[28] D. A. Bonnell, Scanning Probe Microscopy and Spectroscopy: Theory, Techniques, and Applications, JOHN WILEY SONS, INC., 1993. 2.10

[29] F. A. Stevie, C. L. Donley, Introduction to x-ray photoelectron spectroscopy, Journal of Vacuum Science & Technology A 38 (6) (2020) 063204. arXiv:https://pubs.aip.org/avs/jva/article-pdf/doi/10.1116/6.0000412/15822858/063204_1_online.pdf, doi:10.1116/6.0000412.
URL https://doi.org/10.1116/6.0000412 2.5.1, 2.5.1, 2.12, 2.13, 2.14, 4.17

[30] T. Kawagoe, T. Miyamachi, S. Suga, Growth and surface structure of thin co films on au(001) studied by scanning tunneling microscopy, Japanese Journal of Applied Physics 51 (2R) (2012) 025602. doi:10.1143/JJAP.51.025602.
URL https://doi.org/10.1143/JJAP.51.025602 3.1, 5.1, 5.1

[31] T. Kawagoe, T. Miyamachi, M. Someta, T. Kudo, S. Suga, Embedded co nanostructures on au(001) substrate studied by scanning tunneling microscopy, Surface Science 602 (3) (2008) L15–L19. doi:https://doi.org/10.1016/j.susc.2007.12.011.
URL https://www.sciencedirect.com/science/article/pii/S0039602807012071 3.1, 5.1, 5.1

[32] N. Spiridis, T. lzak, M. Zajac, J. Korecki, Ultrathin epitaxial bcc-co films stabilized on au(001)-hex, Surface Science 566-568 (2004) 272–277, proceedings of the 22nd European Conference on Surface Science. doi:https://doi.org/10.1016/j.susc.2004.05.056.
URL https://www.sciencedirect.com/science/article/pii/S0039602804005527 3.1

[33] K. Schouteden, A. Lando, E. Janssens, C. Van Haesendonck, P. Lievens, Morphology and electron confinement properties of co clusters deposited on au(111), New Journal of Physics 10 (8) (2008) 083005. doi:10.1088/1367-2630/10/8/083005.
URL https://doi.org/10.1088/1367-2630/10/8/083005 3.1

[34] S. Padovani, F. Scheurer, J. P. Bucher, Burrowing self-organized cobalt clusters into a gold substrate, Europhysics Letters 45 (3) (1999) 327. doi:10.1209/epl/i1999-00167-2.
URL https://doi.org/10.1209/epl/i1999-00167-2 3.1, 5.1, 5.1

[35] J. de la Figuera, J. E. Prieto, C. Ocal, R. Miranda, Scanning-tunneling-microscopy study of the growth of cobalt on cu(111), Phys. Rev. B 47 (1993) 13043(R)–13046(R). doi:10.1103/PhysRevB.47.13043.
URL https://link.aps.org/doi/10.1103/PhysRevB.47.13043 3.1

[36] M. Wasniowska, N. Janke-Gilman, W. Wulfhekel, M. Przybylski, J. Kirschner, Growth and morphology of cobalt thin films on pd(111), Surface Science 601 (14) (2007) 3073–3081. doi:https://doi.org/10.1016/j.susc.2007.05.011.
URL https://www.sciencedirect.com/science/article/pii/S0039602807005596 3.1

[37] P. Grütter, U. T. Dürig, Growth of vapor-deposited cobalt films on pt(111) studied by scanning tunneling microscopy, Phys. Rev. B 49 (1994) 2021–2029. doi:10.1103/PhysRevB.49.2021.
URL https://link.aps.org/doi/10.1103/PhysRevB.49.2021 3.1

[38] Y. Kuo, P. Yen, W. Chen, S. Chen, S. Yau, In situ scanning tunneling microscopy study of cobalt thin film electrodeposited on pt(111) electrode, Electrochimica Acta 112 (2013) 831–837. doi:https://doi.org/10.1016/j.electacta.2013.05.047.
URL https://www.sciencedirect.com/science/article/pii/S0013468613009523 3.1

[39] E. Lundgren, B. Stanka, M. Schmid, P. Varga, Thin films of co on pt(111): Strain relaxation and growth, Phys. Rev. B 62 (2000) 2843–2851. doi:10.1103/PhysRevB.62.2843.
URL https://link.aps.org/doi/10.1103/PhysRevB.62.2843 3.1

[40] T. Katayama, W. Geerts, Y. Suzuki, D. Fujitani, N. Okuzawa, Oscillation of magneto-optical kerr effect in co ultra-thin films, Journal of Magnetism and Magnetic Materials 156 (1) (1996) 171–172, proceedings of the Second International Symposium on Metallic Multilayers. doi:https://doi.org/10.1016/0304-8853(95)00830-6.
URL https://www.sciencedirect.com/science/article/pii/0304885395008306 3.1

[41] L. Z. Mezey, J. Giber, The surface free energies of solid chemical elements: Calculation from internal free enthalpies of atomization, Japanese Journal of Applied Physics 21 (11R) (1982) 1569. doi:10.1143/JJAP.21.1569.
URL https://doi.org/10.1143/JJAP.21.1569 3.1

[42] V. Stepanyuk, W. Hergert, P. Rennert, Co adatoms on au(100): energetics of site exchange, Computational Materials Science 17 (2) (2000) 309–311. doi:https://doi.org/10.1016/S0927-0256(00)00043-4.
URL https://www.sciencedirect.com/science/article/pii/S0927025600000434 3.1, 5.1, 5.1

[43] J. Unguris, R. J. Celotta, D. T. Pierce, Oscillatory exchange coupling in fe/au/fe(100), Journal of Applied Physics 75 (10) (1994) 6437–6439. arXiv:https://pubs.aip.org/aip/jap/article-pdf/75/10/6437/18666343/6437_1_online.pdf, doi:10.1063/1.356954.
URL https://doi.org/10.1063/1.356954 3.1

[44] P. Carro, G. Andreasen, C. Vericat, M. E. Vela, R. C. Salvarezza, New aspects of the surface chemistry of sulfur on au(111): Surface structures formed by gold-sulfur complexes, Applied Surface Science 487 (2019) 848–856. doi:https://doi.org/10.1016/j.apsusc.2019.05.167.
URL https://www.sciencedirect.com/science/article/pii/S0169433219314758 3.2

[45] M. Yu, H. Ascolani, G. Zampieri, D. P. Woodruff, C. J. Satterley, R. G. Jones, V. R. Dhanak, The structure of atomic sulfur phases on au(111), The Journal of Physical Chemistry C 111 (29) (2007) 10904–10914. doi:10.1021/jp072088+.
URL https://doi.org/10.1021/jp072088+ 3.2

[46] P. Carro, R. C. Salvarezza, Gold adatoms modulate sulfur adsorption on gold, Nanoscale 11 (2019) 19341–19351. doi:10.1039/C9NR05709A.
URL http://dx.doi.org/10.1039/C9NR05709A 3.2

[47] Y. Jiang, X. Liang, S. Ren, C.-L. Chen, L.-J. Fan, Y.-W. Yang, J.-M. Tang, D.-A. Luh, The growth of sulfur adlayers on au(100), The Journal of Chemical Physics 142 (6) (2015) 064708. arXiv:https://pubs.aip.org/aip/jcp/article-pdf/doi/10.1063/1.4907789/14036286/064708_1_online.pdf, doi:10.1063/1.4907789.
URL https://doi.org/10.1063/1.4907789 3.2, 5.2

[48] C. Schlaup, K. Wandelt, In-situ stm study of sulfide adsorption on au(100) in alkaline solution, Surface Science 631 (2015) 165–172, surface Science and Electrochemistry - 20 years later. doi:https://doi.org/10.1016/j.susc.2014.08.006.
URL https://www.sciencedirect.com/science/article/pii/S0039602814002313 3.2, 5.2, 5.2

[49] H. Walen, D.-J. Liu, J. Oh, H. J. Yang, Y. Kim, P. A. Thiel, Identification of aus complexes on au(100), Phys. Chem. Chem. Phys. 18 (2016) 4891–4901. doi:10.1039/C5CP07817B.
URL http://dx.doi.org/10.1039/C5CP07817B 3.2, 5.2, 5.2

[50] B. Fruhberger, M. Grunze, D. J. Dwyer, The formation and stability of sulfhydryl groups on the au(110) surface, The Journal of Physical Chemistry 98 (2) (2002) 609–616. arXiv:https://pubs.acs.org/jpchax/article-pdf/98/2/609/10870768/j100053a041.pdf,

doi:10.1021/j100053a041.
URL https://doi.org/10.1021/j100053a041 3.2

[51] D. M. Jaffey, R. J. Madix, The adsorption of hydrogen sulfide on clean and sulfided au(110), Surface Science 258 (1) (1991) 359–375. doi:https://doi.org/10.1016/0039-6028(91)90930-Q.
URL https://www.sciencedirect.com/science/article/pii/0039602891909300 3.2

[52] F. L. Maza, P. Carro, C. Vericat, K. Kern, R. C. Salvarezza, D. Grumelli, Role of gold adatoms in the adsorption of sulfide species on the gold(001)-hex surface, The Journal of Physical Chemistry C 122 (4) (2018) 2207–2214. arXiv:https://doi.org/10.1021/acs.jpcc.7b11059, doi:10.1021/acs.jpcc.7b11059.
URL https://doi.org/10.1021/acs.jpcc.7b11059 3.2, 5.2

[53] R. Zhao, Z. Wang, Q. Xu, X. Niu, Y. Han, Y. Qin, Q. Wang, Self-supported amorphous iridium oxide catalysts for highly efficient and durable oxygen evolution reaction in acidic media, Electrochimica Acta 391 (2021) 138955. doi:https://doi.org/10.1016/j.electacta.2021.138955.
URL https://www.sciencedirect.com/science/article/pii/S0013468621012457 3.3

[54] J. Yi, W. H. Lee, C. H. Choi, Y. Lee, K. S. Park, B. K. Min, Y. J. Hwang, H.-S. Oh, Effect of pt introduced on ru-based electrocatalyst for oxygen evolution activity and stability, Electrochemistry Communications 104 (2019) 106469. doi:https://doi.org/10.1016/j.elecom.2019.05.018.
URL https://www.sciencedirect.com/science/article/pii/S1388248119301262 3.3

[55] K. Biedermann, M. Gubo, L. Hammer, K. Heinz, Phases and phase transitions of hexagonal cobalt oxide films on ir(100)-(1 Œ 1), Journal of Physics: Condensed Matter 21 (18) (2009) 185003. doi:10.1088/0953-8984/21/18/185003.
URL https://doi.org/10.1088/0953-8984/21/18/185003 3.3

[56] K. Heinz, L. Hammer, Epitaxial cobalt oxide films on ir(100)the importance of crystallographic analyses, Journal of Physics: Condensed Matter 25 (17) (2013) 173001. doi:10.1088/0953-8984/25/17/173001.
URL https://doi.org/10.1088/0953-8984/25/17/173001 3.3

[57] N. Todoroki, H. Tsurumaki, A. Shinomiya, T. Wadayama, Surface microstructures and oxygen evolution properties of cobalt oxide deposited on ir(111) and pt(111) single crystal substrates, Electrochemical Science Advances 3 (6) (2023) e2200007. arXiv:https://chemistry-europe.onlinelibrary.wiley.com/doi/pdf/10.1002/elsa.202200007, doi:https://doi.org/10.1002/elsa.202200007.
URL https://chemistry-europe.onlinelibrary.wiley.com/doi/abs/10.1002/elsa.202200007 3.3

[58] J. Fester, M. Bajdich, A. S. Walton, Z. Sun, P. N. Plessow, A. Vojvodic, J. V. Lauritsen, Comparative analysis of cobalt oxide nanoisland stability and edge structures on three related noble metal surfaces: Au(111), pt(111) and ag(111), Topics in Catalysis 60 (2017) 503–512. doi:10.1007/s11244-016-0708-6.
URL https://doi.org/10.1007/s11244-016-0708-6 3.3

[59] A. Ørsted, S. V. Salling, L. Diekhöner, Unraveling the electronic structure of cobalt oxide nanoislands on au(111), Phys. Rev. B 108 (2023) 165424. doi:10.1103/PhysRevB.108.165424.
URL https://link.aps.org/doi/10.1103/PhysRevB.108.165424 3.3

[60] M. Li, E. I. Altman, Shape, morphology, and phase transitions during co oxide growth on au(111), The Journal of Physical Chemistry C 118 (24) (2014) 12706–12716. arXiv:https://doi.org/10.1021/jp411375w, doi:10.1021/jp411375w.
URL https://doi.org/10.1021/jp411375w 3.3, 5.3

[61] J. Fester, Z. Sun, J. Rodríguez-Fernández, A. Walton, J. V. Lauritsen, Phase transitions of cobalt oxide bilayers on au(111) and pt(111): The role of edge sites and substrate interactions, The Journal of Physical Chemistry B 122 (2) (2018) 561–571, pMID: 28800235. arXiv:https://doi.org/10.1021/acs.jpcb.7b04944, doi:10.1021/acs.jpcb.7b04944.
URL https://doi.org/10.1021/acs.jpcb.7b04944 3.3, 5.3

[62] M. De Santis, A. Buchsbaum, P. Varga, M. Schmid, Growth of ultrathin cobalt oxide films on pt(111), Phys. Rev. B 84 (2011) 125430. doi:10.1103/PhysRevB.84.125430.
URL https://link.aps.org/doi/10.1103/PhysRevB.84.125430 3.3

[63] S. Sindhu, M. Heiler, K.-M. Schindler, W. Widdra, H. Neddermeyer, Growth mechanism and angle-resolved photoemission spectra of cobalt

oxide (coo) thin films on ag(100), Surface Science 566-568 (2004) 471–475, proceedings of the 22nd European Conference on Surface Science. doi:https://doi.org/10.1016/j.susc.2004.06.081.
URL https://www.sciencedirect.com/science/article/pii/S0039602804007496 3.3

[64] A. S. Walton, J. Fester, M. Bajdich, M. A. Arman, J. Osiecki, J. Knudsen, A. Vojvodic, J. V. Lauritsen, Interface controlled oxidation states in layered cobalt oxide nanoislands on gold, ACS Nano 9 (3) (2015) 2445–2453, pMID: 25693621. arXiv:https://doi.org/10.1021/acsnano.5b00158, doi:10.1021/acsnano.5b00158.
URL https://doi.org/10.1021/acsnano.5b00158 3.3, 5.3

[65] F. Srouji, M. Afzaal, J. Waters, P. O'Brien, Single-source routes to cobalt sulfide and manganese sulfide thin films, Chemical Vapor Deposition 11 (2) (2005) 91–94. arXiv:https://onlinelibrary.wiley.com/doi/pdf/10.1002/cvde.200404185, doi:https://doi.org/10.1002/cvde.200404185.
URL https://onlinelibrary.wiley.com/doi/abs/10.1002/cvde.200404185 3.4

[66] A. W. Peters, Z. Li, O. K. Farha, J. T. Hupp, Atomically precise growth of catalytically active cobalt sulfide on flat surfaces and within a metalorganic framework via atomic layer deposition, ACS Nano 9 (8) (2015) 8484–8490. arXiv:https://pubs.acs.org/ancac3/article-pdf/9/8/8484/18067995/nn5b03429.pdf, doi:10.1021/acsnano.5b03429.
URL https://doi.org/10.1021/acsnano.5b03429 3.4

[67] J. Kibsgaard, K. Morgenstern, E. Lægsgaard, J. V. Lauritsen, F. Besenbacher, Restructuring of cobalt nanoparticles induced by formation and diffusion of monodisperse metal-sulfur complexes, Phys. Rev. Lett. 100 (2008) 116104. doi:10.1103/PhysRevLett.100.116104.
URL https://link.aps.org/doi/10.1103/PhysRevLett.100.116104 3.4

[68] M. K. Prabhu, D. Boden, M. J. Rost, J. Meyer, I. M. N. Groot, Structural characterization of a novel two-dimensional material: Cobalt sulfide sheets on au(111), The Journal of Physical Chemistry Letters 11 (21) (2020) 9038–9044, pMID: 32986432. arXiv:https://doi.org/10.1021/acs.jpclett.0c02268, doi:10.1021/acs.jpclett.0c02268.
URL https://doi.org/10.1021/acs.jpclett.0c02268 3.4

[69] K. Morgenstern, E. Lægsgaard, F. Besenbacher, Sintering of cobalt nanoclusters on ag(111) by sulfur: Formation of one-, two-, and three-dimensional cobalt sulfide, Surface Science 602 (3) (2008) 661–670. doi:https://doi.org/10.1016/j.susc.2007.10.046.
URL https://www.sciencedirect.com/science/article/pii/S0039602807010667 3.4

[70] W. Farrow, Considerations for vacuum pump selection (9 2022).
URL https://www.pumpsandsystems.com/article/considerations-vacuum-pump-selection/ 4.1

[71] M. Seidel, Accelerator vacuum (05 2021). doi:10.48550/arXiv.2105.07675. 4.2

[72] G. Binnig, H. Rohrer, Scanning tunneling microscopy, Surface Science 126 (1) (1983) 236–244. doi:https://doi.org/10.1016/0039-6028(83)90716-1.
URL https://www.sciencedirect.com/science/article/pii/0039602883907161 4.4

[73] Y. T. Mohammad Sanchap, Mohammad Tahmasebipour, A linear inch-worm piezomotor with a new configuration: Design considerations, fabrication and characterization, Iranian Journal of Science and Technology, Transactions of Mechanical Engineering 46 (2022) 149–160. doi:10.1007/s40997-020-00409-x. 4.7

[74] R. Hammer, A. Sander, S. Förster, M. Kiel, K. Meinel, W. Widdra, Surface reconstruction of au(001): High-resolution real-space and reciprocal-space inspection, Phys. Rev. B 90 (2014) 035446. doi:10.1103/PhysRevB.90.035446.
URL https://link.aps.org/doi/10.1103/PhysRevB.90.035446 4.4.2, 4.10

[75] A. Trembulowicz, B. Pieczyrak, L. Jurczyszyn, G. Antczak, Coexistence of nanowire-like hex and (1x1) phases in the topmost layer of au(100) surface, Nanotechnology 30 (4) (2018) 045704. doi:10.1088/1361-6528/aaed7f.
URL https://doi.org/10.1088/1361-6528/aaed7f 4.4.2, 4.11

[76] G. M. Trembuowicz A., Sabik A., Au(100) as a template for pentacene monolayer, Molecules (2021). doi:10.3390/molecules26082393. 4.4.2

[77] S. Hofmann, Auger- and X-Ray Photoelectron Spectroscopy in Materials Science, Springer, 2013. 4.7.1, 4.7.1

[78] G. Greczynski, L. Hultman, X-ray photoelectron spectroscopy: Towards reliable binding energy referencing, Progress in Materials Science 107 (2020) 100591. doi:https://doi.org/10.1016/j.pmatsci.2019.100591.
URL https://www.sciencedirect.com/science/article/pii/S0079642519300738 4.18

[79] J. Meyer, I. Baikie, E. Kopatzki, R. Behm, Preferential island nucleation at the elbows of the au(111) herringbone reconstruction through place exchange, Surface Science 365 (1) (1996) L647–L651. doi:https://doi.org/10.1016/0039-6028(96)00852-7.
URL https://www.sciencedirect.com/science/article/pii/0039602896008527 5.1

[80] T.-T. Zhang, Q.-L. Tang, X. Zhang, S.-P. Tang, Q. Wang, Interaction of h2s with au(111) and au(100): A comparative investigation with microkinetic modeling based on dispersion corrected first-principles calculations, Applied Surface Science 682 (2025) 161732. doi:https://doi.org/10.1016/j.apsusc.2024.161732.
URL https://www.sciencedirect.com/science/article/pii/S0169433224024486 5.2

[81] M. H. Heyne, D. Chiappe, J. Meersschaut, T. Nuytten, T. Conard, H. Bender, C. Huyghebaert, I. P. Radu, M. Caymax, J.-F. de Marneffe, E. C. Neyts, S. De Gendt, Multilayer mos2 growth by metal and metal oxide sulfurization, J. Mater. Chem. C 4 (2016) 1295–1304. doi:10.1039/C5TC04063A.
URL http://dx.doi.org/10.1039/C5TC04063A 5.3

[82] M. C. Biesinger, X-ray photoelectron spectroscopy (xps) reference pages - cobalt, https://www.xpsfitting.com/2012/01/cobalt.html, accessed: 17/06/2026 (2009-2021). 5.3

[83] T. F. S. Inc., Table of elements: Cobalt - cobalt x-ray photoelectron spectra, cobalt electron configuration, and other elemental information., https://www.thermofisher.com/br/en/home/materials-science/learning-center/periodic-table/transition-metal/cobalt.html, accessed: 17/06/2026 (2006-2026). 5.3